 doi:10.1111/j.1525-1314.2011.00940.x

P–T–t evolution of granulite facies metamorphism and partial melting in the Winding Stair Gap, Central Blue Ridge, North Carolina, USA

A. K. EL-SHAZLY,[1] C. LOEHN[2] AND R. J. TRACY[2]
[1]*Geology Department, Marshall University, Huntington, WV 25725, USA (elshazly@marshall.edu)*
[2]*Department of Geosciences, Virginia Tech, Blacksburg, VA 24061, USA*

ABSTRACT The Winding Stair Gap in the Central Blue Ridge province exposes granulite facies schists, gneisses, granofelses and migmatites characterized by the mineral assemblages: garnet–biotite–sillimanite–plagioclase–quartz, garnet–hornblende–biotite–plagioclase–quartz ± orthopyroxene ± clinopyroxene and orthopyroxene–biotite–quartz. Multiple textural populations of biotite, kyanite and sillimanite in pelitic schists support a polymetamorphic history characterized by an early clockwise *P–T* path in which dehydration melting of muscovite took place in the stability field of kyanite. Continued heating led to dehydration melting of biotite until peak conditions of 850 ± 30 °C, 9 ± 1 kbar were reached. After equilibrating at peak temperatures, the rocks underwent a stage of near isobaric cooling during which hydrous melt ± K-feldspar were replaced by muscovite, and garnet by sillimanite + biotite + plagioclase. Most monazite crystals from a pelitic schist display patchy zoning for Th, Y and U, with some matrix crystals having as many as five compositional zones. A few monazite inclusions in garnet, as well as Y-rich cores of some monazite matrix crystals, yield the oldest dates of *c*. 500 Ma, whereas a few homogeneous matrix monazites that grew in the main foliation plane yield dates of 370–330 Ma. Culling and analysis of individual spot dates for eight monazite grains yields three age populations of 509 ± 14 Ma, 438 ± 5 Ma and 360 ± 5 Ma. These data suggest that peak-temperature metamorphism and partial melting in the central Blue Ridge occurred during the Salinic or Taconic orogeny. Following near isobaric cooling, a second weaker thermal pulse possibly related to intrusion of nearby igneous bodies resulted in growth of monazite *c*. 360 Ma, coinciding with the Neoacadian orogeny.

Key words: Central Blue Ridge Metamorphism; granulites; monazite ages; partial melting; *P–T* paths; Winding Stair Gap.

Abbreviations: Aln, allanite; Anth, anthophyllite; Ccp, chalcopyrite; L, liquid (melt); Mgt, magnetite; Pn, pentlandite; Ser, sericite; Sill, sillimanite; Ti-Hm, ilmeno-hematite (Titan-hematite); V, vapour; Xn, xenotime.

INTRODUCTION

The Winding Stair Gap (WSG), NW of Franklin, North Carolina (Fig. 1), exposes some of the highest grade metamorphic rocks in the southern Appalachian orogen, and has long been considered part of the thermal axis of Palaeozoic metamorphism (e.g. Carpenter, 1970; Force, 1976; Absher & McSween, 1985; Eckert *et al*., 1989). Although there is general agreement that the WSG rocks underwent partial melting under granulite facies conditions during the Taconic orogeny (e.g. Absher & McSween, 1985; Eckert *et al*., 1989; Miller *et al*., 1996, 1998; Moecher *et al*., 2004), peak *P–T* conditions and evolution remain controversial. Absher & McSween (1985) suggested peak *P–T* conditions of 750–775 °C, 6.5–7 kbar and a segment of near isobaric cooling for WSG rocks, whereas Eckert *et al*. (1989), Moecher & Sharp (1999) and Moecher *et al*. (2004) concluded that the same rocks reached conditions of 800–900 °C, and 8–10 kbar.

The *P–T–t* paths of these rocks are also debated. McLellan *et al*. (1989) suggested that some of the rocks in the WSG were affected by two discrete metamorphic cycles, each with a 'clockwise' *P–T* path. According to McLellan *et al*. (1989), the older of these two cycles was Grenvillian and characterized by peak conditions in the stability field of sillimanite, whereas the younger event was related to a different orogeny and achieved peak conditions in the stability field of kyanite. Eckert *et al*. (1989) suggested that the sillimanite grade WSG rocks record a single metamorphic event in which cooling and decompression resulted in the crystallization of late kyanite. In contrast, Moecher (2000) and Moecher *et al*. (2004) suggested that these rocks had a counterclockwise *P–T* path, with an isobaric cooling segment, to account for the growth of kyanite across the predominant foliation.

The timing of peak metamorphism and partial melting in the central Blue Ridge are also not well constrained. Miller *et al*. (1998) reported concordant

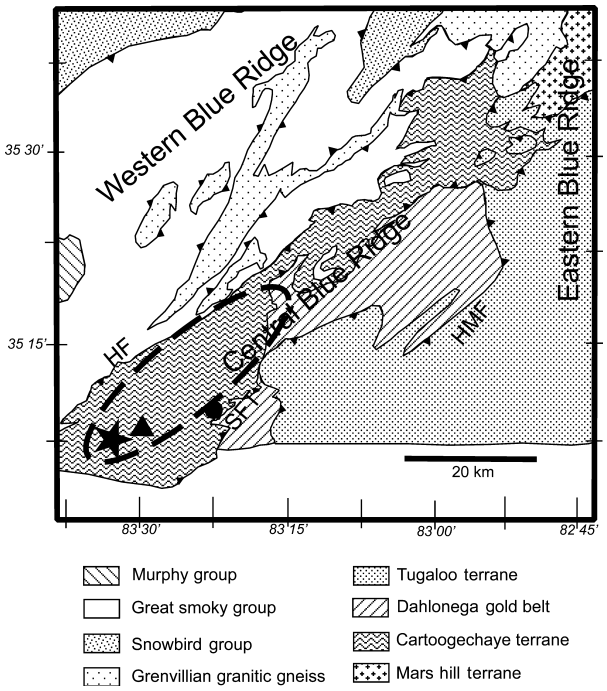

Fig. 1. Simplified geological map of part of the Blue Ridge Province after Hatcher *et al.* (2005) showing the main lithological units in the Western Blue Ridge (Grenvellian - Murphy), other tectonic terranes (Mars Hill - Tugaloo), the location of the Winding Stair Gap road-cut (solid star), the small outcrop east of it (solid triangle) and the town of Franklin (solid circle) along US 64. The dashed line represents the orthopyroxene–in isograd of Carpenter (1970) modified according to the work of Absher & McSween (1985) and Eckert *et al.* (1989). HF, Haysville fault; HMF, Holland Mountain fault; SFT, Shope Fork thrust. Mars Hill terrane: 1.8 Ga pelitic and arenaceous gneisses; Grenvillian Granitic gneiss: 1.15 Ga; Snowbird and Great Smoky Groups: greenschist to amphibolite facies metapsammites and metapelites; Cartoogechaye, Dahlonega Gold belt and Tugaloo Terranes: amphibolite to granulite facies metapsammites, metapelites and metabasites.

U–Pb SHRIMP ages of 495 ± 14 Ma on overgrowths of zircon on detrital grains from pelitic schists from the WSG, which they interpreted as the age of peak metamorphism. Th–Pb SHRIMP ages of 450–430 Ma on complexly zoned monazite from the same rocks were interpreted as recording the age of cooling of this terrane (Miller *et al.*, 1996). Eckert (2002) reported monazite U-Th–Pb dates of 459 ± 7 Ma on monazite from the Central Blue Ridge, including a sample collected 1.8 km from WSG, which he interpreted as the age of peak metamorphism. Using ID-TIMS techniques, Moecher *et al.* (2004) reported concordant U–Pb dates of 458 ± 1 Ma on igneous zircon from garnet-bearing leucosomes from the WSG, which they interpreted as the age of partial melting and of the thermal peak of metamorphism. Moecher *et al.* (2004) also concluded that the leucosomes represent plagioclase-rich cumulates remaining after the fractionation of a more felsic melt that migrated out of the system.

In this study, we present petrographic and chemical data, themobarometric estimates, and monazite U–Th–Pb dates for a variety of samples from the WSG. Because U–Th–Pb dating of monazite is non-destructive (i.e. it preserves textural information), and has a spatial resolution superior to that of the ion microprobe, dates obtained by this method can be interpreted in the context of metamorphic, anatectic and deformational events affecting the area, even though the increased spatial resolution comes at the expense of decreased temporal resolution. Therefore, the main objectives of this study are to constrain (i) peak *P–T* conditions of metamorphism at WSG; (ii) the conditions and triggers of partial melting; (iii) the *P–T* paths of WSG rocks, that is, whether clockwise or counterclockwise; and (iv) the timing of peak metamorphism and partial melting and their effects on monazite chemistry and dating.

GEOLOGICAL SETTING

The WSG (35°07′20.64″N, 83°32′42.34″W) is a 370 m long road-cut located ~18 km west of Franklin along an E–W stretch of US highway 64 (Fig. 1). Units exposed in this road-cut were originally considered part of the Eastern Blue Ridge (e.g. Absher & McSween, 1985; Eckert *et al.*, 1989). However, according to recent maps by Hatcher (2002) and Hatcher *et al.* (2005), the WSG is now considered part of the Cartoogechaye terrane of the Central Blue Ridge (Fig. 1), as this terrane was found to contain some Grenville basement rocks, and consists of psammitic granofelses and pelitic schists the protoliths of which were deposited off the Laurentian margin, where they mixed with mafic and ultramafic material.

Rocks exposed in the WSG outcrop include pelitic schists and gneisses, quartzofeldspathic gneisses and granofelses, orthopyroxenites and calcsilicate boudins. The pelitic and quartzofeldspathic schists and gneisses were affected by partial melting, which is manifested by leucosomes that range from small millimetre-wide pods (Fig. 2a) to centimetre- and tens of centimetre-wide layers alternating with melanosomes. This gives rise to stromatic migmatites (Fig. 2b), which locally grade into minor diatexites (Fig. 2c). Vein-like plagioclase-rich leucosomes (Fig. 2d) crosscutting the stromatic migmatites and the main structural features of the WSG are also common. Moecher *et al.* (2004) interpreted these relations as indicating two generations of leucosomes; an early generation consisting of plagioclase + quartz + K-feldspar ± garnet ± rutile in the stromatic migmatites, and a later generation of 'dioritic' dykes.

Absher & McSween (1985) considered the WSG rocks to represent metamorphosed shales, greywackes, basic igneous intrusions or interlayered volcanics, all belonging to the Tallulah Falls Formation which is considered part of the Proterozoic, rift-related Coweeta Group (e.g. Hatcher, 1973). These authors

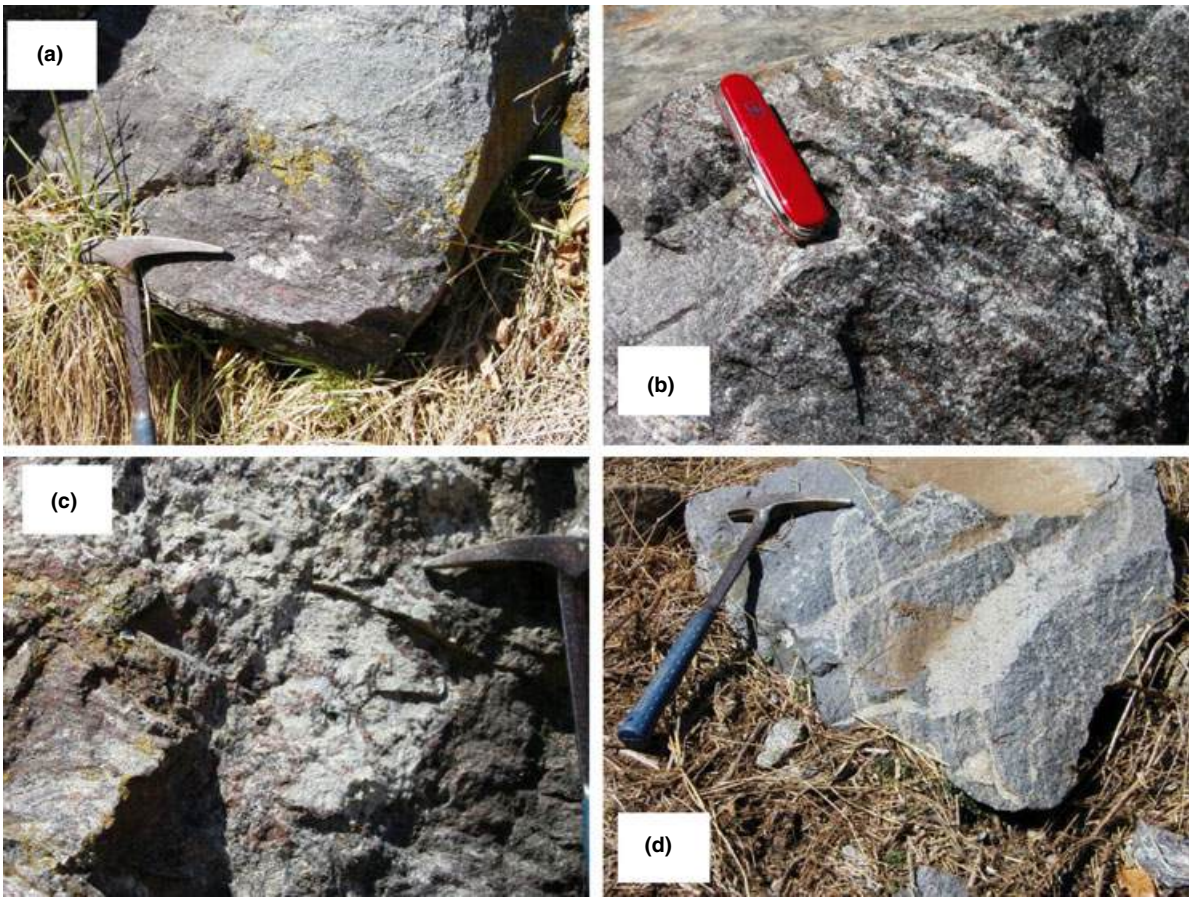

Fig. 2. Types of leucosomes/migmatites at Winding Stair Gap: (a) leucocratic pod in sillimanite schist; (b) stromatic migmatites; (c) diatexites; (d) leucosome dykelets crosscutting Grt–Hb–Bt granofels.

interpreted the orthopyroxenites as part of ophiolitic slices similar to those exposed elsewhere in the Eastern and Central Blue Ridge. Eckert *et al*. (1989) mapped the WSG units as part of the Coleman River Formation, whereas Hatcher (2010) considered it to be part of the Ridgepole formation (both units also of the Coweeta Group). In all cases, the WSG units are considered to have been metamorphosed during the Taconic orogeny (e.g. Dallmeyer, 1975; Miller *et al*., 1998).

Several deformational events are considered to have affected WSG (e.g. Absher & McSween, 1985; Eckert *et al*., 1989). The earliest deformation (D_1) is represented by tight upright to steeply inclined folds plunging NW, and interpreted to have caused the boudinage structure of the calcsilicates. The second deformational event (D_2) was the strongest, and resulted in tight to isoclinal flow folds with steeply dipping NE to NW striking axial planes. D_2 is considered to have accompanied the main metamorphic event, producing the predominant foliation defined by 'peak' metamorphic biotite + sillimanite during the Taconic orogeny (e.g. Hatcher & Butler, 1979; Massey & Moecher, 2005). Later deformational events (D_3 and D_4) produced upright crenulations that deformed some of the leucosomes crosscutting the main foliation, and may have been responsible for some of the observed ptygmatic folding (Eckert *et al*., 1989). Although D_3 and D_4 are interpreted to have post-dated the crystallization of 'late' kyanite and retrograde muscovite in some leucosomes (Eckert *et al*., 1989), these late deformational events are described by Absher & McSween (1985) as neither widespread nor pervasive.

ANALYTICAL TECHNIQUES

Mineral analysis

In this study, we focus on 19 samples (Table 1) collected from the WSG and another outcrop ~1 km to the east along highway 64 (35°07′46.9″N, 83°32′17.96″W). The samples selected for detailed analysis included sillimanite–garnet–biotite schists and gneisses, garnet–biotite–hornblende granofelses, orthopyroxenites and associated leucosomes. Table 1 lists the modal contents of the samples studied. Microprobe analysis was carried out on a JEOL JSM 5310 LV scanning electron microscope equipped with a Link Pentafet EDS at

Table 1. Modal contents of representative samples.

	Grt	Bt	Opx	Cpx	Hb	Anth	Plag	Qtz	Kfs	Sill	Ky	Ilm	Rt	Relict	Retrograde	Accessories
Pelitic schists and gneisses																
WSG-2	30–35	20–25	–	–	–	–	30	10	tr	2–3	tr	2–3	tr	St, Ky	Ank, Cal, Musc, Py, Chl, Ser, Chl(5)	Mnz, Zrn, Xn, Aln, Ap, Mnz
WSG-2b	15–20	25–30	–	–	–	–	10	15	5	10–15	3–5	2–3	tr(in Grt)	St, Ky	Ms(10), Py Ms(3)	Ap, Xn
WSG-7(m)	60	5	–	–	–	–	15	5	–	tr	–	2			Chl(10), Ttn	Mnz, Zrn, Ap
WSG-44	20	5–7	–	–	–	–	45–50	20	–	1–2	–	3	–	–	–	Ap Hc, Mgt, Hem
WSG-14	10–15	20–25	–	–	–	–	30	15	tr	5–7	1	1–2	tr	Rt, Ky	Ms(7)	Mnz, Xn, Zrn, Aln
WSG-15	20–25	20–25	–	–	–	–	7	7	15	10	1–2	5	–	Ky	Ms(10–15)	Mnz, Ap
WSG-29(m)	25–30	20	–	–	–	–	5	10	–	20–25	–	7–10	tr	–	Chl	Hc, Mnz
S9110(m)	30	30–35	–	–	–	–	1	3	–	10–15	–	5	tr	–	–	Mnz
Leucosomes																
Stromatic																
WSG-27b	tr	10–15	–	–	–	–	70	< 5	–	1	1	1	1	–	Ms (3)	Xn
WSG-35	15	7	–	–	–	–	60	15	–	1	1–2	1–2	1–2	–		Zrn, Mnz(?), Ap
WSG-37	tr	tr	–	–	–	–	25	70	–	–	–	–	1	–	Ms(3), Cc	Ap
Non-stromatic																
WSG-7(I)	10	5	–	–	–	–	25–30	50	–	5	–	tr	tr	–	Chl	
WSG-29(I)	7–10	7–10	–	–	–	–	60	7–10	–	3–5	–	5	–	–	–	Hc, Mnz
WSG-30	tr	7	–	–	–	–	15–20	60–65	?	1	–	3	–	–	Ms(2)	Mnz, Ap
S9110 (l)	tr	2	–	–	–	–	5	10	80	tr	1–2	–	–	–	Ms(3)	Ap(2), Czo
WSG-43	–	2	–	–	2	–	70	15–20	–	–	–	–	–	–	Chl (2)	Zrn, Mnz
Grt-Hb-Bt granofelses																
WSG-1	5–10	10	–	tr	20–25	–	45	10	–	tr	–	1	–	–	Cal	Zrn, Ap, Ttn, Czo(2), Aln, Zrn,
WSG-41	10	10	–	–	20–25	–	35–40	5	–	tr	–	2	tr	–	Cal	Mnz, Ap
WSG-21	7–10	7–10	7	5	5	5–10	40	5	–	tr	–	5	–	–	Ank, Tlc, Chl	Ap(5), Zrn, Py(4)
WSG-39	5	5	–	–	5	15	50	15	–	tr	–	7	tr	–		Zrn, Mnz, Ap
'Orthopyroxenites'																
WSG-23	–	15–20	50	–	–	5	–	15	–	–	–	3	1–2	–	Cal	Py, Ccp, Pn, Mnz
WSG-25	–	10	65	–	–	5	–	15	–	–	–	–	1–2	–	Cal	Py, Zrn, Ap

Marshall University. Analytical conditions were 20 kV operating voltage, 95 mAmp condenser lens current, a working distance of 20 mm, and a beam size of 2 μm. Beam current intensity was monitored on pure Co, with a calibration performed every 2 h maintaining a count rate of 26–27 kcps, and a dead time of ≤25%. Standardization was performed on well-characterized Smithsonian Institution standards, all mounted on the same sample holder. Standards included microcline (Si, K, Al), scapolite (Na, Al, Cl), Kakanui hornblende (Ti), Kakanui pyrope (Mg, Si, Al), diopside (Ca, Mg), chromite (Cr), Roberts Victor garnet 1 and 2 (Ca, Si), Rockport fayalite (Fe, Mn), Johnstown hypersthene (Fe), gahnite (Zn) and INGAR garnet (Fe, Mn). These and additional standards (e.g. Kakanui augite and Lake County plagioclase) were routinely analysed as unknowns to check on the quality of the analyses. Analytical data were processed using LINK ISIS 3.1 software and a ZAF correction. Precision is estimated at 1–2% for all oxide weight percentage values, and 10% or better for Na_2O.

Mineral formulae were calculated on the basis of 8, 12 and 22 oxygen atoms per formula unit (apfu) for feldspar, garnet and biotite respectively, assuming all Fe as Fe^{2+} for the latter two minerals. Formulae for anthophyllite/cummingtonite and hornblende were calculated based on 15 cations less Na and K, and 13 cations less Na + K + Ca respectively, using 'Amphibol' (Richard & Clarke, 1990). Formulae for pyroxene, ilmenite/hematite and magnetite were all calculated using 'Minfile' (Afifi & Essene, 1988) based on 6, 3 and 4 oxygen apfu respectively, with Fe^{3+} estimated stoichiometrically.

U–Th–Pb monazite geochronology

In situ monazite geochronology was performed at Virginia Polytechnic Institute and State University in the Department of Geosciences Electron Microbeam Laboratory with a Cameca SX50 electron probe microanalyser (EPMA) equipped with four wavelength-dispersive spectrometers (WDS), secondary electron and backscatter electron (BSE) detectors, and an energy-dispersive X-ray spectrometer (EDS). Individual monazite grains were BSE imaged on a Camscan Series II SEM at 20 kV and a working distance of 35 mm, to identify strong Th and U compositional zoning patterns, fractures and minor imperfections, including mineral inclusions. Additional BSE images were taken at 20×, 80× and 180× magnification for potential post-analysis correlation of monazite microtextures with macroscopic deformational fabric(s).

Monazite grains were selected for high resolution X-ray mapping of Y, Th, U and Ca based on size, grain integrity and microstructural relation to surrounding minerals. Beam-scan mode WDS compositional maps (512 × 512 pixels) were created with an acceleration voltage of 15 kV and beam current of

300 nA, to allow for compositional heterogeneity and zoning pattern identification. Analytical traverse lines were positioned based on elemental mapping, to provide a sufficient sampling within and across distinct compositional domains in order to characterize potential relationships between compositional and age domains with statistical reliability. Analysis along such traverses was preferred over targeting specific compositional domains to minimize bias on age population selection, and hence on ultimate age interpretations.

Electron microprobe (EPM) U–Th–Pb dating of monazite utilizes an accelerating potential of 15 kV and a regulated beam current of 200 nA, a peak counting time of 900 s, and upper and lower background position counting times of 450 s each (i.e. 30 min per analysis). Four WDS spectrometers were used for the simultaneous measurement of X-ray lines Y $L\alpha$ (on TAP), Th $M\alpha$ (on PET), U $M\alpha$ (on PET) and Pb $M\alpha$ (on PET). Spatial resolution (spot size) of $\sim$2.5 μm was achieved with the above analytical conditions, compared with a theoretical minimum at 15 kV and 200 nA of 2.2 μm (Castaing, 1960). A fixed chemical matrix of major and minor elements (P, Ce, La, Nd, Sm, Gd, Dy) was used for matrix ZAF corrections. Matrix corrections were done using a PAP routine (Pouchou & Pichoir, 1991), and a standard correction of Pb $M\alpha$ for the spectral interference from Y $L\alpha$ was performed as a post-analysis correction (Åmli & Griffin, 1975; Williams *et al*., 1999). To avoid analytical bias, and to minimize any uncertainty related to absolute error in standard concentrations, only well-characterized natural or synthetic standards were used for elemental calibration. These include synthetic YAG ($Y_3Al_5O_{12}$) for yttrium, synthetic annealed ThO_2 for Th (from Cannon Microprobe, Inc.), synthetic depleted UO_2 for uranium (from Sandia National Lab), and a well-characterized natural pyromorphite ($Pb_5[PO_4]_3Cl$) for lead (from the Harvard Mineralogical Museum).

Data were initially synthesized using a Microsoft Excel^{TM} spreadsheet constructed to recalculate Pb concentration, after correcting for spectral interferences of Y on Pb $M\alpha$. Using the data synthesis and error analysis technique of Loehn (2009), individual Th, U and Y-corrected Pb concentrations obtained for each analysed spot were entered into a subsequent spreadsheet designed to calculate 2σ relative and absolute concentration errors based on the 1σ concentration uncertainties reported by the electron microprobe (cf. Cochérie & Albaréde, 2001 for comparison). Data were then sorted in descending order according to the Pb relative error, rounded to a whole integer, and new worksheets were created, each for a subpopulation with a unique value of Pb relative error. Relative and absolute errors for each new subpopulation were then compiled to yield an average relative and absolute error for each element (2σ). These worksheets were then processed through the EPMA Excel add-in program (Pommier *et al*., 2003), and a final spreadsheet was compiled (cf. Appendix S1) and used to generate appropriate discrimination plots using the ISOPLOT3 program (Ludwig, 2003). These plots were used to identify age populations (cf. Loehn, 2009), and screened with the mean standard-weighted deviation (MSWD) criterion of McIntyre *et al*. (1966) and Wendt & Carl (1991). Age uncertainty was calculated using the individual analysis 1σ elemental error (Th, U, and Pb) to calculate 2σ relative and absolute errors for processing data through the EPM Excel^{TM} add-in program (Pommier *et al*., 2003). All errors in EPM data discussed in the text and depicted graphically in the figures are at the 2σ level (95% confidence), including the error at the centroid of an age regression in Th/Pb–U/Pb space or Th–Pb CHIME plots (Suzuki & Adachi, 1991; Cochérie & Albaréde, 2001).

Although the age uncertainty on an individual spot analysis on monazite ranges from $\pm$25 to $\pm$100 Ma, ages obtained using the above analytical and culling procedures have lower uncertainties and have been shown to be typically within 2σ error of ages obtained by ion microprobe (IP; including SHRIMP) (Tracy *et al*., 2005; Tracy & Loehn, 2006). Examples of similar age samples included in these inter-lab studies were three monazite grains from a study on the Black Mountain granite (Ratcliffe *et al*., 2001); monazite grain 6 age of 368 $\pm$ 12 Ma by IP *v*. 355 $\pm$ 3 Ma by EPMA; monazite grain 7 age of 376 $\pm$ 12 Ma by IP *v*. 358 $\pm$ 4 Ma by EPMA; monazite grain 10 age of 386 $\pm$ 12 Ma by IP *v*. 390 $\pm$ 7 Ma by EPMA.

PETROGRAPHY AND MINERAL CHEMISTRY

Quartzofeldspathic and pelitic schists and gneisses

The quartzofeldspathic/semipelitic rocks with gneissic to granofelsic textures are most abundant in both outcrops, whereas the pelitic schists and gneisses are limited to the eastern and central parts of the WSG road-cut. Both rock types are migmatized, and characterized by the 'peak' mineral assemblage: garnet–biotite–sillimanite–plagioclase–quartz–ilmenite–rutile $\pm$ K-feldspar. Many samples contain texturally early staurolite and kyanite. Rutile, although ubiquitous, is a minor phase that is typically included in garnet, whereas K-feldspar occurs as rare inclusions in garnet or plagioclase. Other minerals include accessory monazite, zircon, apatite $\pm$ xenotime $\pm$ magnetite $\pm$ Ti-hematite $\pm$ Fe–Mg–Al-rich spinel (herein loosely referred to as hercynite), and retrograde chlorite, muscovite, calcite, ankerite and pyrite. The predominant foliation, defined by the orientation of peak minerals in the gneisses and schists, is typically tightly folded. Leucosomes, whether concordant or discordant with the main foliation, are predominantly plagioclase and quartz, along with smaller amounts of biotite, kyanite and sillimanite $\pm$ garnet $\pm$ K-feldspar, although the latter is a predominant phase in a few stromatic samples (e.g. WSG-15; S9110).

Accessory minerals include apatite, zircon, xenotime, ilmenite, titan-hematite and rutile ± monazite ± clinozoisite. Randomly oriented, medium-grained crystals of retrograde muscovite are ubiquitous.

Garnet

Garnet ranges from fine-grained (80 μm) equant crystals in some leucosomes (e.g. WSG-7; Fig. 3a) to coarse-grained (0.5 cm) clusters elongated with the predominant foliation in mesocratic rocks (WSG-2b; Fig. 3b). Many crystals are characterized by resorbed outlines (e.g. WSG-2; WSG-14), and are surrounded by thin films of quartz + plagioclase (± K-feldspar ± muscovite) separating them from biotite (Fig. 3c). Whereas garnet in many leucosomes is almost devoid of inclusions, most garnet in melanosomes contains abundant inclusions of plagioclase, biotite, quartz, sillimanite, ilmenite, rutile and apatite ± monazite ± xenotime ± allanite. In some of the pelitic schists, garnet occurring along the leucosome–melanosome contact also contains inclusions of hercynite + magnetite + ilmenite + Ti-hematite + biotite + sillimanite ± K-feldspar (e.g. WSG-14; WSG-29; Fig. 3d). The common orientation of these inclusions suggests syn-deformational crystallization of their host garnet in many cases, although pressure shadows (e.g. WSG-2) and a helicitic texture (e.g. WSG-2b) for a few samples indicate episodes of pre- and post-deformational crystallization respectively. Fractures in garnet are typically filled with one or more of the minerals calcite, ankerite, chlorite, pyrite, muscovite and biotite. The latter is typically of the green variety, even when the predominant matrix biotite is brown to reddish brown (e.g. WSG-37).

Compositionally, the garnet is homogeneous, displaying only a minor increase in Fe, Ca and Mn, and decrease in Mg along the rims, or next to inclusions of biotite (Fig. 4; Table 2). In the melanosomes, garnet is almandine-rich (X_{Alm} = 0.65–0.78) with significant amounts of pyrope (X_{Prp} = 0.14–0.27) but minor grossular (X_{Grs} = 0.038–0.095) and spessartine (X_{Sps} = 0.013–0.023). In WSG-14, garnet is slightly richer in spessartine (X_{Sps} = 0.05–0.1), and poorer in grossular (X_{Grs} < 0.05), but is otherwise unzoned as indicated by X-ray maps (available upon request). In the leucosomes, garnet is characterized by a higher pyrope content (X_{Prp} = 0.29 ± 0.04), and a

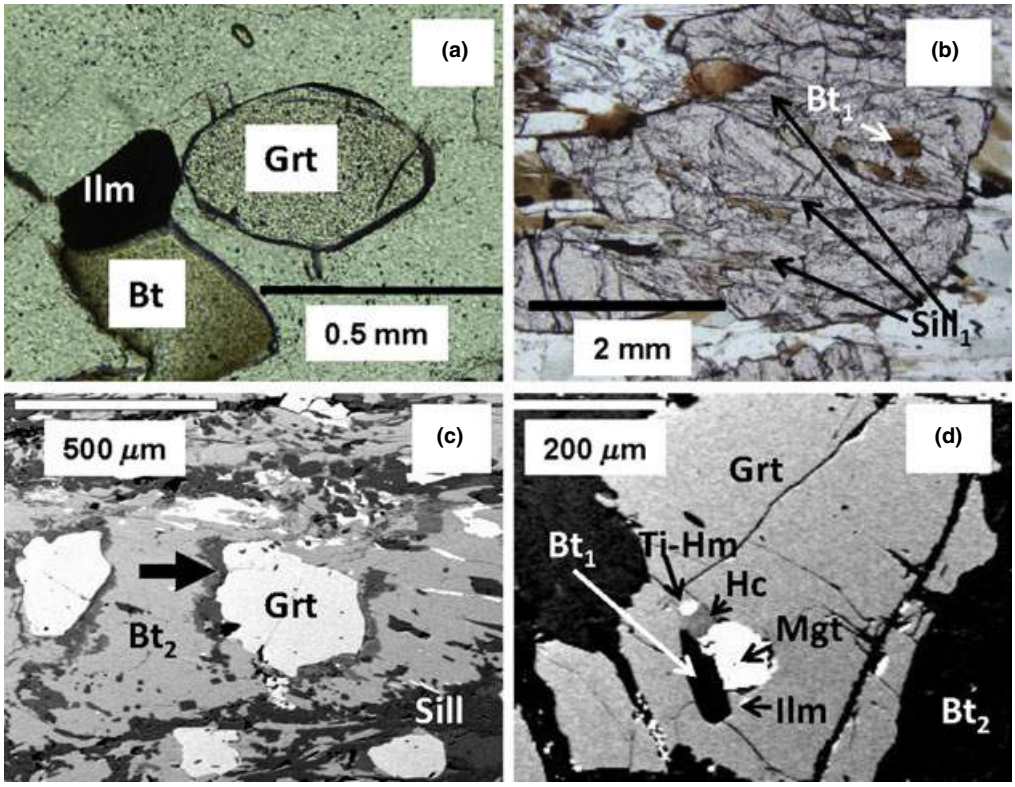

Fig. 3. Selected textural relations in pelitic schists and leucosomes: (a) Rounded, inclusion-free garnet in leucosome; sample WSG-27b, plane-polarized light (ppl); (b) porphyroblasts of elongated garnet with inclusions of fibrolite; sample WSG-2b, ppl; (c) back-scattered electron image (BSEI) showing thin selvages of quartz + plagioclase ± muscovite (indicated by thick black arrows) rimming garnet with resorbed outlines, sample WSG-14; (d) BSEI of garnet with inclusions of hercynite, Ti-hematite, ilmenite, magnetite and biotite; sample WSG-14.

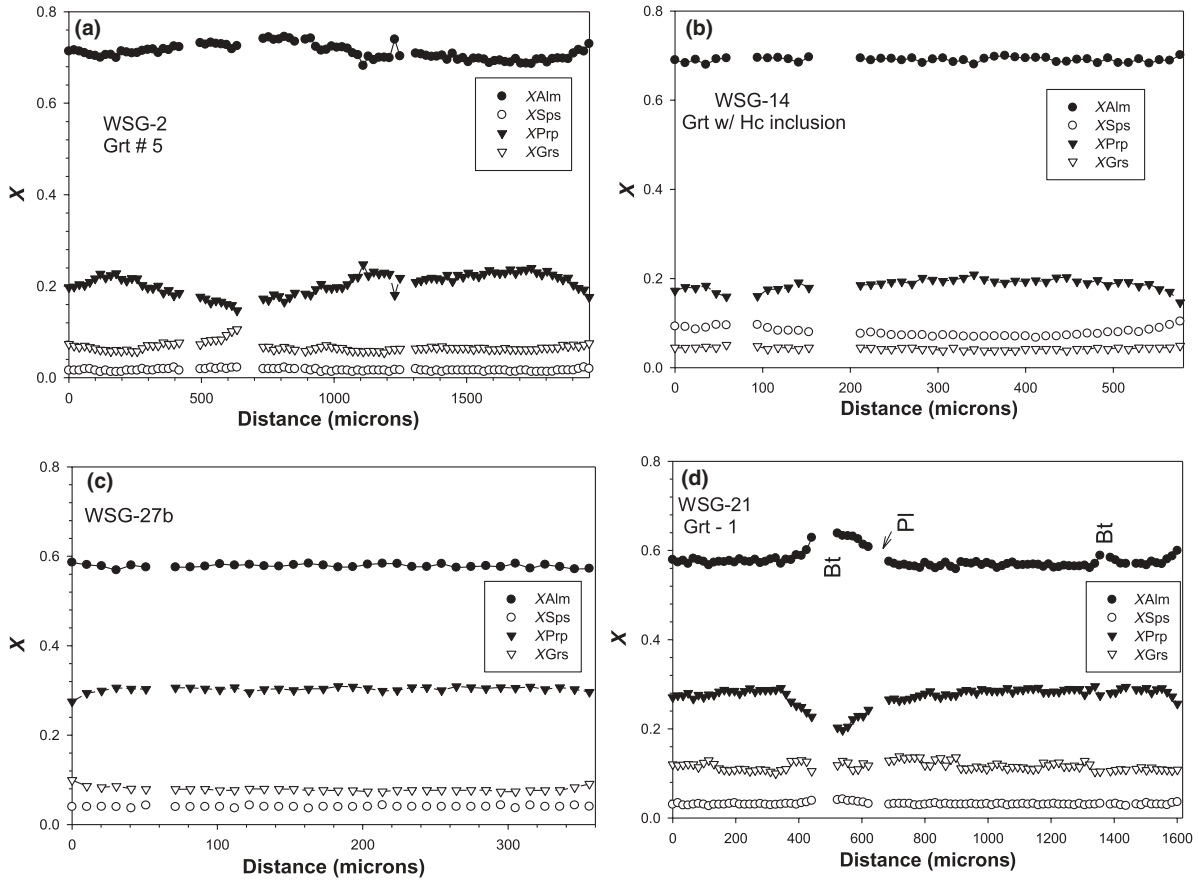

Fig. 4. Zoning profiles in garnet from (a) quartzofeldspathic gneiss, (b) pelitic schist, (c) leucosome and (d) two pyroxene-bearing garnet–biotite–hornblende granofels. Breaks represent locations of inclusions or fractures.

lower almandine component (X_{Alm} = 0.62 ± 0.03; Table 2). These results are very similar to those reported by Moecher *et al.* (2004), although these authors also reported a Ca-rich core in coarse-grained garnet from one of their leucosomes.

Biotite

Biotite occurs as (i) inclusions in garnet (Bt_1; e.g. Fig. 3b,d) and kyanite, sometimes oriented with sillimanite ($Sill_1$) to define a distinct internal foliation (S_i); (ii) coarse-grained crystals (Bt_{2a}) frequently rimmed by ilmenite, and either sheared into mica fish (Fig. 5a), or aligned with coarse-grained kyanite oriented (S_1) at a high angle to the main foliation plane (S_2; Fig. 5b); (iii) as coarse- to fine-grained crystals (Bt_{2b}) oriented with prismatic sillimanite and fibrolite ($Sill_2$) in the main foliation plane (S_2) sometimes 'decapitating' garnet (Fig. 5c) in the pelitic layers; and (iv) as irregular (commonly green) crystals along fractures and rims of garnet in both pelitic and quartzofeldspathic layers (Bt_3; Table 3). In the leucosomes, the small amount of biotite typically occurs in isolated restitic masses or as randomly oriented or radiating crystals. Many of these crystals have distinct rinds of a symplectic intergrowth of biotite and either K-feldspar (WSG-15) or plagioclase (WSG-14), and are commonly overgrown by a muscovite–plagioclase symplectite (Fig. 5d). Inclusions of zircon, monazite, xenotime, rutile (sometimes rimmed by ilmenite), ilmenite, plagioclase and quartz are common in matrix biotite (Bt_2).

Despite the occurrence of several textural varieties of biotite (sometimes with different colours) in the same sample, they do not show distinct chemical differences (Table 3; Fig. S1). On the basis of 22 oxygen apfu, most biotite has a relatively restricted composition with Al^{iv} = 2.4–2.6, Al^{vi} = 0.5–0.9; Mg# (Mg/(Mg + Fe)) = 0.5–0.6, and Ti^{vi} = 0.15–0.25; quite similar to average biotite compositions from amphibolite facies rocks (Guidotti, 1984). Nevertheless, a few inclusions in garnet are characterized by high Mg# (~0.62) or Ti^{vi} values (0.3–0.44), whereas most biotite filling in fractures in garnet is typically Fe-rich and Ti-poor (Mg# < 0.5; Fig. S1; Table 3). Relative to biotite in the quartzofeldspathic gneisses, green biotite in pelitic schists is characterized by a higher Ti^{vi} (0.26–0.42), which is negatively correlated with Mg# (Fig. S1). Leucosomal biotite is very similar

Table 2. Representative garnet analyses.

	WSG-2				WSG-2b					WSG-14								WSG27b				WSG-41						
	1 med 15	1 med 18	Grt2 38_core	Grt2 2_rim	Grt3_sp5 9 rim	Grt2_Sp5 2	Grt1 _Sp3 1 core	Grt3_p 1_rim	Grt1_Sp1 1 core	Grt1_sp1 2_rim	Grt1b 5 core	Grt8 26 core	Grt8 25 rim	Spot 6 43 core	54 core	53 rim	Retro* 73 grt	Spot 1 3 rim	4 core	5 core	8 rim	1 core	3 rim	Grt3 18 core	19 rim	Grt4 29 core	30 rim	36 rim
SiO_2	36.92	36.59	37.25	37.67	36.96	36.43	36.47	35.66	35.82	35.95	36.98	37.51	37.20	36.91	36.87	36.74	36.64	39.28	38.61	36.88	37.55	37.59	38.09	38.01	37.11	37.85	37.26	37.74
TiO_2	0.09	0.00	0.00	0.15	0.03	0.00	0.03	0.04	0.10	0.02	0.11	0.13	0.00	0.10	0.05	0.07	0.14	0.14	0.07	0.05	0.00	0.18	0.19	0.20	0.11	0.19	0.18	0.13
Al_2O_3	21.86	22.02	21.74	22.00	21.43	20.96	22.06	20.59	21.51	21.93	21.61	21.96	21.66	21.68	20.79	20.98	21.01	22.03	21.69	20.70	21.17	21.31	21.74	21.71	21.26	21.66	21.37	21.47
Cr_2O_3	0.02	0.06	0.00	0.02	0.09	0.04	0.00	0.11	0.00	0.00	0.00	0.01	0.00	0.04	0.09	0.03	0.00	0.06	0.07	0.09	0.09	0.05	0.07	0.00	0.10	0.03	0.06	0.11
FeO	33.16	32.20	32.96	33.05	34.09	35.51	34.74	34.26	29.72	29.89	30.68	30.95	30.78	32.20	32.50	32.37	30.52	27.10	27.07	30.61	29.69	26.68	26.52	26.40	26.16	26.76	28.89	26.79
MnO	0.91	0.94	0.86	1.00	0.70	0.83	0.87	0.94	4.55	4.86	4.71	4.86	5.14	3.53	3.26	4.18	6.41	1.91	1.97	2.80	2.65	1.30	1.25	0.86	0.88	1.02	1.49	1.02
MgO	4.52	5.02	5.31	4.00	3.21	3.28	4.83	4.01	4.95	5.02	4.41	4.34	4.24	4.74	5.12	4.27	3.12	7.94	7.97	4.94	5.16	5.98	5.91	7.26	6.76	6.62	5.27	6.84
CaO	2.73	2.34	2.62	3.55	3.58	2.51	1.46	1.41	1.71	1.72	1.59	1.59	1.62	1.65	1.48	1.80	2.08	3.03	2.83	3.15	3.83	6.26	6.33	5.66	5.74	5.82	5.39	5.53
Total	100.20	99.15	100.74	101.44	100.10	99.56	100.45	97.02	98.37	99.40	100.10	101.36	100.64	100.85	100.16	100.44	99.92	101.50	100.29	99.22	100.14	99.34	100.09	100.05	98.11	99.95	99.92	99.63
Si	2.94	2.93	2.94	2.96	2.96	2.96	2.91	2.95	2.91	2.89	2.95	2.96	2.96	2.93	2.95	2.95	2.96	3.00	2.99	2.97	2.97	2.96	2.97	2.96	2.95	2.96	2.95	2.96
Ti	0.01	0.00	0.00	0.01	0.00	0.00	0.00	0.00	0.01	0.00	0.01	0.01	0.00	0.01	0.00	0.00	0.01	0.01	0.00	0.00	0.00	0.01	0.01	0.01	0.01	0.01	0.01	0.01
Al	2.05	2.08	2.02	2.04	2.02	2.00	2.07	2.01	2.06	2.08	2.03	2.04	2.03	2.03	1.96	1.98	2.00	1.98	1.98	1.96	1.98	1.98	2.00	1.99	1.99	1.99	1.99	1.98
Cr	0.00	0.00	0.00	0.00	0.01	0.00	0.00	0.01	0.00	0.00	0.00	0.00	0.00	0.00	0.01	0.00	0.00	0.00	0.00	0.01	0.01	0.00	0.00	0.00	0.01	0.00	0.00	0.01
Fe	2.21	2.16	2.18	2.17	2.29	2.41	2.32	2.37	2.02	2.01	2.05	2.04	2.05	2.14	2.18	2.17	2.06	1.73	1.75	2.06	1.97	1.76	1.73	1.72	1.74	1.75	1.91	1.76
Mn	0.06	0.06	0.06	0.07	0.05	0.06	0.06	0.07	0.31	0.33	0.32	0.32	0.35	0.24	0.22	0.28	0.44	0.12	0.13	0.19	0.18	0.09	0.08	0.06	0.06	0.07	0.10	0.07
Mg	0.54	0.60	0.63	0.47	0.38	0.40	0.57	0.50	0.60	0.60	0.53	0.51	0.50	0.56	0.61	0.51	0.38	0.90	0.92	0.59	0.61	0.70	0.69	0.84	0.80	0.77	0.62	0.80
Ca	0.23	0.20	0.22	0.30	0.31	0.22	0.12	0.13	0.15	0.15	0.14	0.13	0.14	0.14	0.13	0.15	0.18	0.25	0.23	0.27	0.33	0.53	0.53	0.47	0.49	0.49	0.46	0.46
Fe/Mg	4.12	3.60	3.46	4.62	5.95	6.08	4.04	4.74	3.37	3.34	3.90	4.00	4.07	3.82	3.57	4.25	5.42	1.91	1.91	3.47	3.23	2.50	2.52	2.04	2.17	2.27	3.08	2.20
X_{Alm}	0.73	0.71	0.71	0.72	0.76	0.78	0.75	0.77	0.66	0.65	0.68	0.68	0.67	0.69	0.69	0.70	0.67	0.58	0.58	0.66	0.64	0.57	0.57	0.56	0.56	0.57	0.62	0.57
X_{Sps}	0.02	0.02	0.02	0.02	0.02	0.02	0.02	0.02	0.10	0.11	0.11	0.11	0.11	0.08	0.07	0.09	0.14	0.04	0.04	0.06	0.06	0.03	0.03	0.02	0.02	0.02	0.03	0.02
X_{Prp}	0.18	0.20	0.20	0.16	0.13	0.13	0.19	0.16	0.19	0.19	0.17	0.17	0.17	0.18	0.19	0.16	0.12	0.30	0.30	0.19	0.20	0.23	0.23	0.27	0.26	0.25	0.20	0.26
X_{Grs}	0.08	0.07	0.07	0.10	0.10	0.07	0.04	0.04	0.05	0.05	0.05	0.04	0.05	0.05	0.04	0.05	0.06	0.08	0.08	0.09	0.11	0.17	0.17	0.15	0.16	0.16	0.15	0.15

*Retro: Grt in retrograde rind with Pl, Ms, Qtz.

to that in melanosomes, but shows a more restricted compositional range (Ti^{vi} = 0.34–0.41; Mg# = 0.55–0.58; Al^{iv} = 2.67–2.71).

Feldspar

Plagioclase is the most common feldspar in pelitic schists and gneisses and in most leucosomes (Table 1). It contains some inclusions of biotite, sillimanite, apatite, monazite, as well as minor K-feldspar (WSG-14), and chlorite (WSG-2b). Finer-grained plagioclase crystals are included in biotite and garnet. Plagioclase also occurs as symplectic intergrowths with retrograde muscovite ± biotite (WSG-14; Fig. 5d) or quartz (WSG-35; Fig. 5f), and as thin rims surrounding kyanite in some leucosomes (S9110). All analysed crystals are homogeneous with X_{An} = 0.35–0.45, and X_{Or} < 0.01 (Table 4). K-feldspar is the predominant phase in only a few stromatic metatexites, where it may be perthitic (e.g. WSG-15). Otherwise, K-feldspar occurs only as inclusions in garnet or plagioclase.

Other minerals

Sillimanite is ubiquitous, occurring as oriented inclusions in garnet ($Sill_1$; Fig. 3b), as coarse- to fine-grained crystals ($Sill_2$) defining the main foliation S_2 (Fig. 5c), or as minute fibrous crystals along the grain boundaries of garnet (Fig. 5e) and plagioclase ($Sill_3$; Fig. 5f). Kyanite occurs as bladed crystals oriented with Bt_{2a} at an angle to the main foliation (Ky_1; Fig. 5b), and that sometimes overgrew staurolite topotactically (Fig. 6a). Kyanite also occurs as strongly deformed crystals oriented in the main foliation plane, where it is overgrown by coarse-grained sillimanite (Fig. 6b). In leucosomes, kyanite is deformed and either rimmed by quartz or overgrown by fibrolite (Ky_2; Fig. 6c). Staurolite is rare, found mostly as inclusions in garnet (Fig. 6d). Ilmenite is usually the only iron oxide in most samples, but in some pelitic schists it overgrows magnetite and titan-hematite, in addition to occurring as exsolution lamellae in the latter (Fig. 6e; Table 5). Rutile most commonly occurs as inclusions in garnet (Fig. 6f) or plagioclase. It also occurs as matrix crystals rimmed by ilmenite in schists and granofelses, or as an intergranular phase in some leucosomes (e.g. WSG-35). Muscovite is a common retrograde mineral, typically occurring as coarse-grained xenoblasts with resorbed outlines, especially in leucosomes. Although it is usually randomly oriented where it overgrows plagioclase feldspar and coarse-grained biotite (Bt_2), some muscovite is oriented in the main foliation plane S_2. Chlorite is rare, commonly replacing biotite. Monazite, apatite, and xenotime are common accessories, occurring as inclusions in garnet and plagioclase, or as intergranular phases in the matrix. Zircon and allanite occur in some samples as intergranular matrix phases. Zinc-bearing hercynite is a rare mineral that occurs as inclusions in garnet (Fig. 3d) or as a

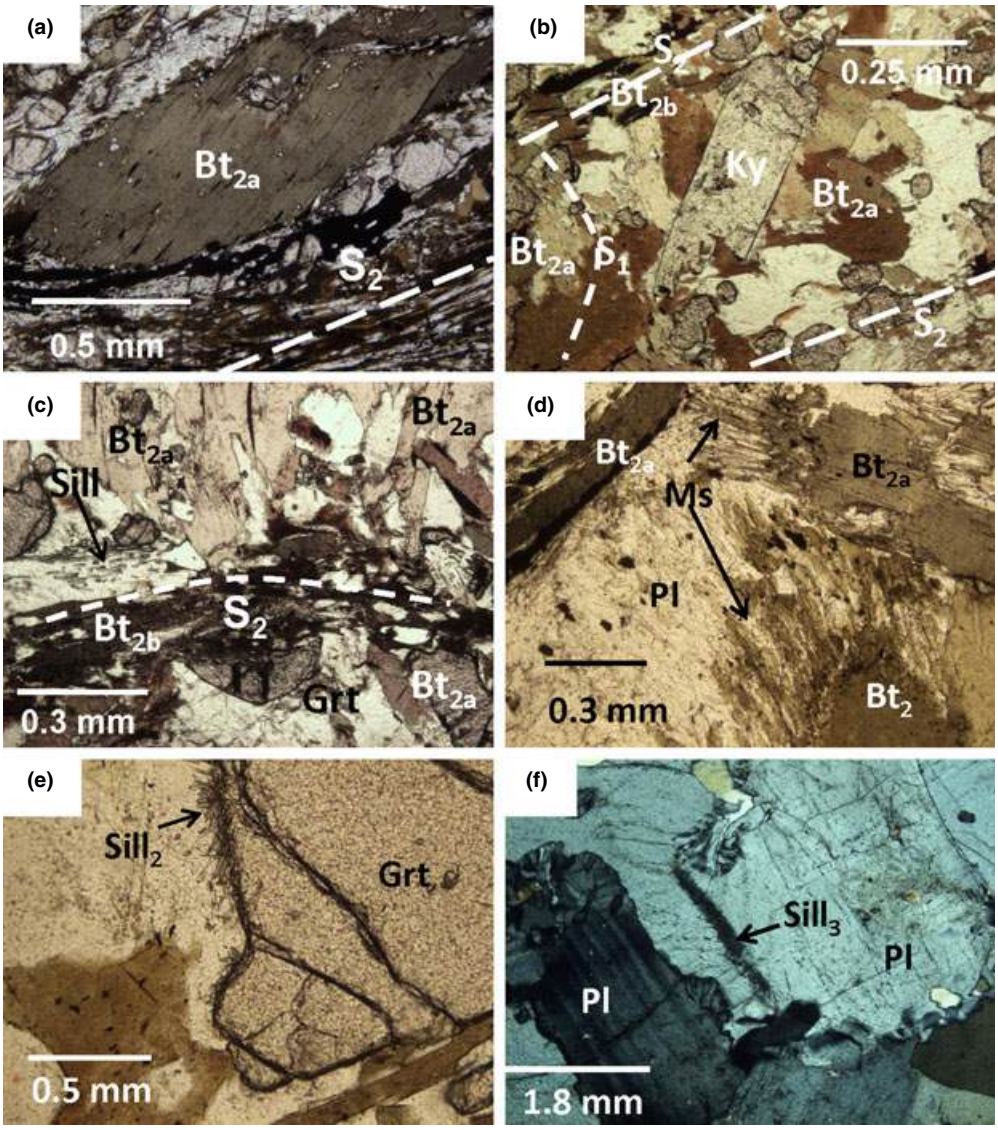

Fig. 5. Selected textural relations in pelitic schists, leucosomes, and granofelses: (a) Biotite$_{2a}$ mica fish rimmed by ilmenite and oriented at an angle to the main foliation S_2 defined by fine-grained sillimanite and biotite$_{2b}$, WSG-14, ppl; (b) Kyanite crystals (Ky_1) crosscut by main foliation S_2 defined by Sill and Bt_{2b}, WSG-14, ppl; (c) Fibrolite ($Sill_2$) and Bt_{2b} oriented along the main foliation plane (S_2) and crosscutting garnet; WSG-14, ppl; (d) Symplectic intergrowth of muscovite and plagioclase partially replacing biotite, WSG-14, ppl; (e) Sillimanite ($Sill_2$) along garnet grain boundaries, WSG-2, ppl; (f) Myrmekitic texture in plagioclase and fibrolite ($Sill_3$) along plagioclase grain boundaries; WSG-35, crossed polarizers (xpl).

minor intergranular matrix phase that concentrates along the leucosome–melanosome boundary in WSG-14 and WSG-29.

Garnet–hornblende granofelses and orthopyroxenites

The garnet–hornblende granofelses are predominated by plagioclase coexisting with smaller amounts of hornblende, garnet, biotite, quartz and occasional pyroxene (Table 1). The abundance of plagioclase along with the significant modal content of quartz and biotite, lead us to suggest that these rocks probably represent metamorphosed greywackes rather than mafic igneous rocks. All samples contain minor amounts of fibrolite, typically occurring along garnet rims, or plagioclase grain boundaries. Although characterized by a granofelsic texture, most of the hornblende and biotite crystals are oriented to define a very weak foliation. The orthopyroxenites are rare, exposed only in the western part of the WSG road-cut (Absher & McSween, 1985). These coarse-grained granofelsic rocks are predominated by orthopyroxene with significant amounts of biotite, quartz and ilmenite, as well as rare plagioclase, sulphides, apatite, zircon, monazite and retrograde calcite (Table 1). Despite the Mg-rich nature of these orthopyroxenites and the

Table 3. Representative biotite analyses.

	WSG-2				WSG2b		WSG-14					WSG-27b	WSG-41	WSG-21	WSG-23	
	9 Bt1	9b core Bt1	6 Bt2b	f21 3 fracture	6 Bt2a	20 Bt2b core	81 Bt1	66 Bt2	27 Bt 2	22 Bt2b rim	21 Bt 3	8	17	35	18 matrix	39 incl
SiO_2	37.31	37.21	37.42	35.97	37.10	36.38	35.57	34.21	34.73	35.49	35.08	36.14	34.98	37.22	38.07	38.47
TiO_2	4.92	4.83	1.54	1.39	1.64	1.55	2.50	3.36	2.90	2.65	2.31	3.02	1.79	2.92	3.07	2.01
Al_2O_3	17.41	17.48	19.13	18.47	19.46	18.56	20.21	17.58	18.41	18.80	18.78	17.31	17.11	15.56	15.20	15.17
Cr_2O_3	0.00	0.07	0.07	0.00	0.00	0.10	0.08	0.01	0.00	0.08	0.10	0.03	0.00	0.32	0.80	0.51
FeO	15.59	15.80	16.64	17.98	16.46	17.81	14.52	18.44	17.12	16.95	17.02	14.90	18.62	12.96	10.15	8.91
MnO	0.00	0.00	0.00	0.00	0.06	0.00	0.07	0.00	0.00	0.09	0.07	0.06	0.00	0.04	0.05	0.06
MgO	11.41	11.43	11.83	10.96	12.07	12.13	13.17	11.07	11.53	11.76	11.44	14.03	12.36	16.01	18.08	19.09
CaO	0.00	0.00	0.00	0.00	0.00	0.00	0.00	0.00	0.00	0.00	0.00	0.00	0.12	0.00	0.00	0.00
Na_2O	0.00	0.00	0.00	0.00	1.37	1.14	1.04	1.12	0.86	1.07	1.21	1.12	0.98	0.80	0.80	0.65
K_2O	9.62	9.73	9.72	9.39	9.41	9.31	9.47	9.54	9.18	9.51	9.47	9.45	8.41	9.49	9.51	9.76
Total	96.26	96.55	96.35	94.16	97.57	96.98	96.63	95.33	94.73	96.40	95.48	96.06	94.37	95.32	95.73	94.63
Si^{iv}	5.51	5.49	5.53	5.49	5.43	5.41	5.23	5.24	5.29	5.30	5.30	5.37	5.37	5.52	5.55	5.63
Al^{iv}	2.49	2.51	2.47	2.51	2.57	2.59	2.77	2.76	2.71	2.70	2.70	2.63	2.63	2.48	2.45	2.37
Al^{vi}	0.54	0.53	0.86	0.82	0.79	0.66	0.73	0.41	0.59	0.62	0.65	0.40	0.46	0.24	0.16	0.25
Ti^{vi}	0.55	0.54	0.17	0.16	0.18	0.17	0.28	0.39	0.33	0.30	0.26	0.34	0.21	0.33	0.34	0.22
Cr^{+3}	0.00	0.01	0.01	0.00	0.00	0.01	0.01	0.00	0.00	0.01	0.01	0.00	0.00	0.04	0.09	0.06
Fe^{+3}	0.00	0.00	0.00	0.00	0.00	0.00	0.00	0.00	0.00	0.00	0.00	0.00	0.00	0.00	0.00	0.00
Fe^{+2}	1.92	1.95	2.06	2.30	2.02	2.21	1.79	2.36	2.18	2.12	2.15	1.85	2.39	1.61	1.24	1.09
Mn^{+2}	0.00	0.00	0.00	0.00	0.01	0.00	0.01	0.00	0.00	0.01	0.01	0.01	0.00	0.01	0.01	0.00
Mg	2.51	2.51	2.61	2.50	2.64	2.69	2.89	2.53	2.62	2.62	2.58	3.11	2.83	3.54	3.93	4.17
Ca	0.00	0.00	0.00	0.00	0.00	0.00	0.00	0.00	0.00	0.00	0.00	0.00	0.02	0.00	0.00	0.00
Na	0.00	0.00	0.00	0.00	0.39	0.33	0.30	0.33	0.25	0.31	0.35	0.32	0.29	0.23	0.23	0.18
K	1.81	1.83	1.83	1.83	1.76	1.77	1.78	1.86	1.78	1.81	1.83	1.79	1.65	1.80	1.77	1.82
Mg#	0.57	0.56	0.56	0.52	0.57	0.55	0.62	0.52	0.55	0.55	0.55	0.63	0.54	0.69	0.76	0.79

occurrence of minor pentlandite, their SiO_2 and K_2O contents (50–54%; 0.5–1.2% respectively; A. El-Shazly, unpublished data) are too high for a mantle peridotite. We therefore suggest that these rocks represent metasedimentary rocks that have undergone significant partial melting and loss of feldspar to the extracted melt (cf. Stevens *et al.*, 1997).

Garnet

Garnet occurs as medium- to coarse-grained (2 mm to >1 cm) subhedral crystals with a few inclusions of one or more of the following minerals: quartz, plagioclase, hornblende, anthophyllite, biotite, clinopyroxene, ilmenite, apatite, allanite or zircon. Many crystals have resorbed outlines, and are partially rimmed by fibrolite, ilmenite, plagioclase or hornblende. Most garnet has a prominent set of cracks and fractures filled with hornblende and biotite (WSG-39), or quartz, calcite and oxychlorite (WSG-41). Compositionally, this garnet is homogeneous, showing only a minor increase in Fe/Mg at the outermost rims (Fig. 4d). Compared with garnet in WSG pelitic and quartzofeldspathic schists and gneisses, it is more enriched in pyrope and grossular, having an average composition of $X_{Alm} = 0.57 \pm 0.02$, $X_{Sps} = 0.02 \pm 0.003$, $X_{Prp} = 0.26 \pm 0.04$, $X_{Grs} = 0.14 \pm 0.04$ (Fig. 4d; Table 2).

Biotite

Biotite is a common mineral in the WSG granofelses, occurring as subhedral crystals in apparent textural equilibrium with hornblende and plagioclase in most samples. It typically contains a few inclusions of ilmenite, apatite, monazite, zircon and hornblende, and in one sample (WSG-1), titanite. Compositionally, these crystals are quite similar to those occurring in the metapelites and quartzofeldspathic mica schists, with $Al^{vi} = 0.3–0.6$, $Ti = 0.2–0.3$ and $Mg\# = 0.5–0.8$ (Fig. S1; Table 3). In some granofelses (e.g. WSG-21), inclusions in garnet have a higher Mg# and Al^{vi} compared with matrix crystals (Fig. S1). In the orthopyroxenites, biotite constitutes 10–20% of the rock mode, occurring as subhedral crystals with inclusions of ilmenite, rutile, apatite ± pyrite, or as inclusions in orthopyroxene (Fig. 6g). Unlike biotite in all other rock types, biotite in the orthopyroxenites is Mg-rich ($Mg\# > 0.7$), and relatively enriched in Ti (0.3–0.4), although biotite inclusions in orthopyroxene have a significantly lower Ti and slightly higher Mg# compared with matrix crystals (Fig. S1; Table 3).

Amphibole

Hornblende (tschermakite to tschermakitic hornblende; Table 6) constitutes up to 25% of some granofelses (Table 1). It occurs as subhedral crystals oriented to define a very weak foliation, and contains inclusions of apatite, quartz, plagioclase and oriented ilmenite. In a few samples (e.g. WSG-1), hornblende is rimmed by biotite or ilmenite, but in most samples it appears to be in textural equilibrium with plagioclase, biotite and quartz (e.g. WSG-41). Anthophyllite or cummingtonite ($Al^{iv} \leq 0.3$; $Mg\# = 0.7 \pm 0.01$;

Table 6) is restricted to biotite and/or garnet-rich layers of some granofelses (e.g. WSG-39, WSG-21) where it appears to have formed with calcite or ankerite at the expense of pyroxene (± biotite, hornblende and garnet; Fig. 6h). It also occurs along the rims of orthopyroxene in the orthopyroxenites.

Pyroxene

Orthopyroxene constitutes the bulk of orthopyroxenites, occurring as coarse-grained crystals with inclusions of quartz, biotite, ilmenite, chalcopyrite, pentlandite and rutile. With the exception of submicroscopic blebs of quartz oriented along their cleavage planes, this orthopyroxene is homogeneous with an average composition of 73.2 ± 1% enstatite, 26.4 ± 1% ferrosilite and 0.27 ± 0.4% wollastonite, and total Al_2O_3 of 1.8–1.9% by weight (Table 7). Most crystals are rimmed by anthophyllite ± calcite.

A few granofelses (e.g. WSG-21) contain two pyroxenes; a hypersthene (57 ± 1% enstatite, 42 ± 1% ferrosilite and 0.5 ± 0.05% wollastonite) and a subcalcic clinopyroxene (50 ± 4% enstatite, 25 ± 3% ferrosilite, 6 ± 3% wollastonite, 9 ± 0.5% jadeite + aegirine; Table 7). These two pyroxenes are homogeneous, and appear to be in textural equilibrium with biotite, garnet, hornblende and plagioclase. Whereas the hypersthene is sometimes rimmed by anthophyllite/cummingtonite, the subcalcic clinopyroxene is partially to completely replaced by anthophyllite ± ankerite (Fig. 6h).

Other minerals

Plagioclase (X_{An} = 0.55 ± 0.01, X_{Ab} = 0.43 ± 0.01, X_{Or} = 0.02 ± 0.01) occurs as medium-grained (0.5–1 mm) homogeneous crystals in the granofelses, but is a minor phase in some orthopyroxenites where it occurs only as inclusions in orthopyroxene. Ilmenite is also homogeneous with the composition X_{IIm} = 0.93–0.94 and X_{Hem} = 0.04–0.08 (Table 5). Rutile occurs as ubiquitous inclusions in orthopyroxene and anthophyllite in the orthopyroxenites, but is a rare mineral in the granofelses, occurring only as inclusions in ilmenite. Clinozoisite is a minor product of plagioclase alteration in WSG-41. Calcite/ankerite and rare titanite are interpreted as retrograde minerals. The sulphides pyrite, chalcopyrite and pentlandite all occur as highly irregular inclusions in orthopyroxene and anthophyllite in the orthopyroxenites.

P–T CONDITIONS OF METAMORPHISM

Lack of major element zoning in garnet analysed in the different rock types from the WSG outcrop suggests that temperatures of metamorphism exceeded 650 °C, the temperature at which growth zoning is typically homogenized by volume diffusion (e.g. Tracy, 1982). The occurrence of orthopyroxene in some

Table 4. Representative analyses of feldspar.

	WSG-2						WSG-2b				WSG-14						WSG-27b						WSG-41				
	1	2	11	10	12	27	15 in Grt	17 in Grt	21 in Grt	10 in Grt	12	13	60 core	61r rim	56 rind	57	64	78 Kspar	2c core	3r rim	5r rim	8 c core	14 r rim	15 c core	8	9	10	13
SiO_2	55.22	54.21	59.30	60.09	58.82	58.63	59.92	60.12	58.71	62.67	61.47	62.94	59.54	60.35	57.95	60.13	60.07	64.05	56.82	58.43	59.05	58.59	57.91	58.3	56.1	56.58	56.79	55.89
Al_2O_3	28.04	28.56	26.00	26.06	25.65	25.92	25.85	26.21	25.90	18.32	24.85	24.67	25.01	24.59	25.74	24.24	25.05	19.79	25.82	26.34	26.64	26.33	25.76	26.41	27.53	28.18	28.25	28.08
FeO	0.16	0.12	0.17	0.30	0.37	0.04	0.21	0.33	0.36	0.35	0.07	0.06	0.08	0.13	0.19	0.07	0.07	0.26	0.04	0.13	0.05	0.08	0.05	0.06	0.02	0.00	0.01	0.00
MgO	0.58	0.62	0.74	0.73	0.62	0.40	0.72	0.69	0.50	1.20	0.57	0.63	0.68	0.46	0.75	0.52	0.73	0.9	0.08	0.11	0.07	0.1	0.11	0.09	0.97	0.75	0.82	0.98
CaO	8.44	7.76	7.42	7.07	7.01	7.22	7.02	7.26	7.12	0.00	6.11	5.54	6.21	5.53	7.18	5.34	6.02	0.03	8.88	9.1	9.01	9.1	8.51	9.03	9.4	9.75	9.81	9.76
Na_2O	7.05	7.96	5.69	5.69	5.54	5.29	5.51	5.54	5.54	1.25	5.54	5.71	6.39	6.54	5.79	6.73	6.23	1.64	5.5	5.49	5.56	5.54	5.7	5.48	4.21	4.32	4.15	4.08
K_2O	0.07	0.06	0.02	0.05	0.01	0.04	0.00	0.00	0.05	14.49	0.29	0.38	0.13	0.16	0.08	0.13	0.19	13.75	0.29	0.39	0.26	0.19	0.21	0.55	0.04	0.1	0.08	0.09
Total	99.57	99.30	99.35	99.99	98.01	97.53	99.22	100.14	98.20	97.53	98.90	99.92	98.04	97.76	97.68	97.16	98.36	100.4	97.43	99.99	100.6	99.93	98.25	99.92	98.27	99.7	99.99	98.95
Si	2.50	2.46	2.65	2.66	2.66	2.66	2.67	2.66	2.65	2.95	2.73	2.76	2.69	2.72	2.63	2.73	2.70	2.93	2.61	2.61	2.62	2.62	2.63	2.61	2.54	2.53	2.53	2.52
Al	1.49	1.53	1.37	1.36	1.37	1.38	1.36	1.37	1.38	1.01	1.30	1.28	1.33	1.31	1.38	1.30	1.33	1.07	1.40	1.39	1.39	1.39	1.38	1.39	1.47	1.49	1.48	1.49
Fe	0.01	0.00	0.01	0.01	0.01	0.00	0.01	0.01	0.01	0.01	0.00	0.00	0.00	0.01	0.00	0.00	0.00	0.01	0.00	0.00	0.00	0.00	0.00	0.00	0.00	0.00	0.00	0.00
Mg	0.04	0.04	0.05	0.05	0.04	0.03	0.05	0.05	0.03	0.08	0.04	0.04	0.05	0.03	0.05	0.04	0.05	0.06	0.01	0.01	0.00	0.01	0.01	0.01	0.07	0.05	0.05	0.07
Ca	0.41	0.38	0.35	0.34	0.34	0.35	0.33	0.34	0.34	0.00	0.29	0.26	0.30	0.27	0.35	0.26	0.29	0.00	0.44	0.44	0.44	0.44	0.41	0.43	0.46	0.47	0.47	0.47
Na	0.62	0.70	0.49	0.49	0.49	0.46	0.48	0.47	0.48	0.11	0.48	0.49	0.56	0.57	0.51	0.59	0.54	0.15	0.49	0.48	0.48	0.48	0.50	0.48	0.37	0.37	0.36	0.36
K	0.00	0.00	0.00	0.00	0.00	0.00	0.00	0.00	0.00	0.87	0.02	0.02	0.01	0.01	0.00	0.01	0.01	0.80	0.02	0.02	0.01	0.01	0.01	0.03	0.00	0.01	0.00	0.01
X_{An}	0.40	0.35	0.42	0.41	0.41	0.43	0.41	0.42	0.41	0.00	0.37	0.34	0.34	0.32	0.41	0.30	0.35	0.00	0.46	0.47	0.47	0.47	0.45	0.46	0.55	0.55	0.57	0.56
X_{Ab}	0.60	0.65	0.58	0.59	0.59	0.57	0.59	0.58	0.58	0.12	0.61	0.63	0.64	0.67	0.59	0.69	0.64	0.16	0.52	0.51	0.52	0.52	0.54	0.51	0.45	0.44	0.43	0.43
X_{Or}	0.00	0.00	0.00	0.00	0.00	0.00	0.00	0.00	0.00	0.88	0.02	0.03	0.01	0.01	0.00	0.01	0.01	0.84	0.02	0.02	0.01	0.01	0.01	0.03	0.00	0.01	0.00	0.01

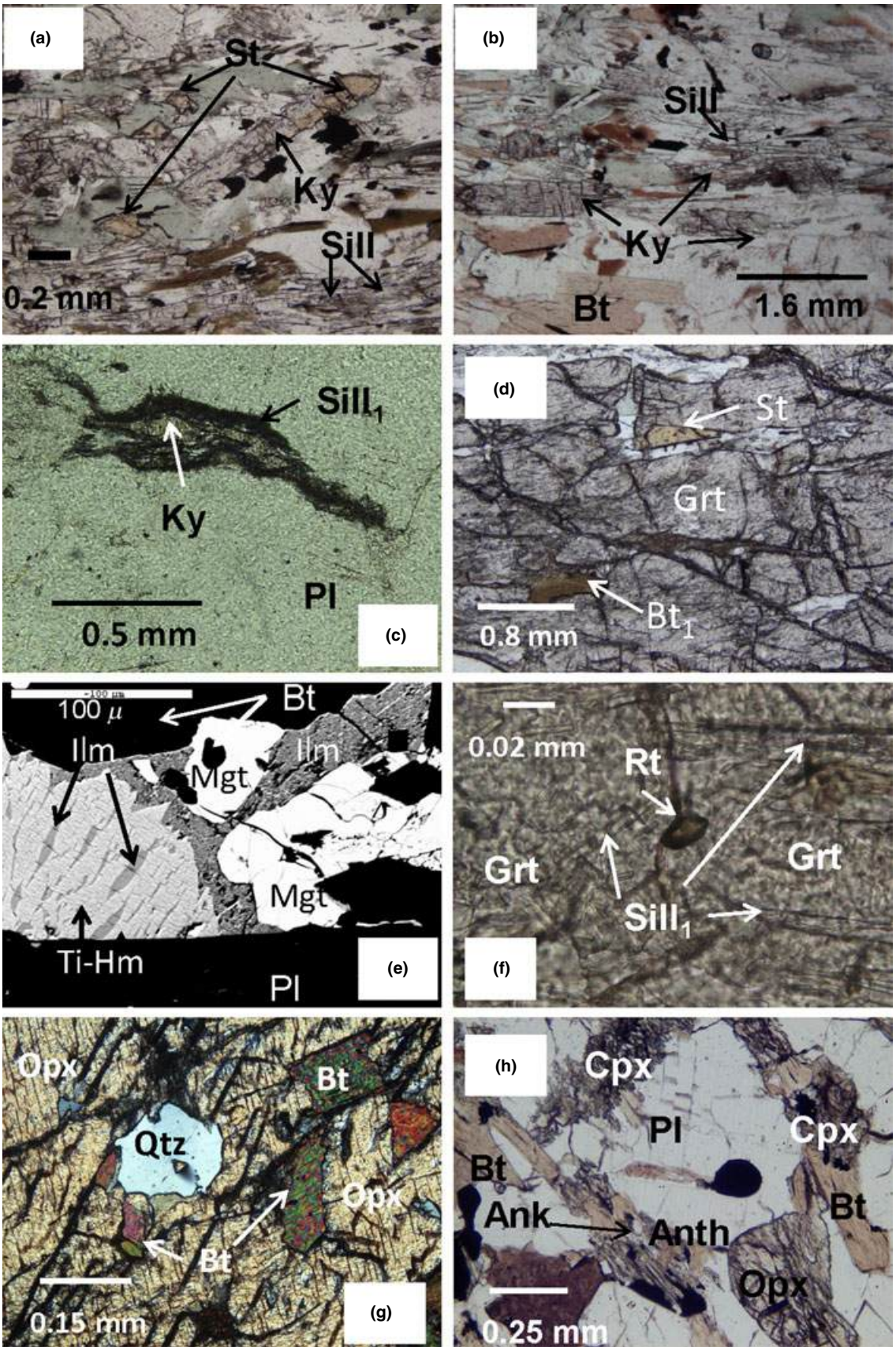

Table 5. Representative analyses of Fe-oxides.

	WSG-2		WSG-2b	WSG-23	WSG-21	WSG-41	WSG-14						
	Ilm									Ti-Hm		Mgt	Hc
	12 incl	13	12 incl	13	13	29	40	12	83	25	84	11	55
SiO_2	0.00	0.00	0.00	0.00	0.58	0.61	0.49	0.93	0.72	0.73	0.53	1.12	0.00
TiO_2	49.34	47.96	50.28	51.70	47.61	46.81	49.51	48.25	42.38	14.45	15.39	0.09	5.26
Al_2O_3	0.00	0.00	0.00	0.00	0.51	0.61	0.49	0.62	0.53	0.70	0.52	0.88	53.70
Cr_2O_3	0.11	0.18	0.14	0.15	0.18	0.10	0.00	0.23	0.23	0.27	0.58	0.02	0.43
Fe_2O_3	5.78	7.23	3.11	0.51	7.27	7.98	3.77	1.52	15.43	72.12	68.20	65.51	0.00
FeO	43.90	42.53	44.98	46.25	40.21	40.72	43.83	42.76	35.53	12.73	13.48	32.05	23.21
MnO	0.00	0.00	0.08	0.00	0.35	0.33	0.65	0.08	0.27	0.00	0.00	0.00	0.00
MgO	0.00	0.00	0.00	0.00	1.65	0.99	0.35	0.75	0.98	0.57	0.47	0.42	0.00
CaO	0.00	0.00	0.00	0.00	0.00	0.00	0.00	0.00	0.00	0.00	0.00	0.00	0.00
V_2O_5	n.d.	n.d.	n.d.	n.d.	n.d.	n.d.	n.d.	n.d.	n.d.	n.d.	n.d.	0.00	0.00
ZnO	n.d.	n.d.	n.d.	n.d.	n.d.	0.00	0.00	n.d.	n.d.	n.d.	n.d.	0.16	7.91
	99.13	97.90	98.59	98.61	98.36	98.15	99.09	95.14	96.07	101.57	99.17	100.25	90.51
	3 Oxygen											4 Oxygen	
Si	0.00	0.00	0.00	0.00	0.02	0.02	0.01	0.02	0.02	0.02	0.01	0.04	0.00
Ti	0.94	0.93	0.97	1.00	0.91	0.90	0.94	0.95	0.82	0.28	0.30	0.00	0.12
Al	0.00	0.00	0.00	0.00	0.02	0.02	0.02	0.02	0.02	0.02	0.02	0.04	1.97
Cr	0.00	0.00	0.00	0.00	0.00	0.00	0.00	0.00	0.00	0.01	0.01	0.00	0.01
Fe^{+3}	0.11	0.14	0.06	0.01	0.14	0.15	0.07	0.03	0.30	1.38	1.34	1.87	0.00
Fe^{+2}	0.94	0.93	0.97	1.00	0.85	0.87	0.93	0.94	0.80	0.27	0.30	1.02	0.60
Mn	0.00	0.00	0.00	0.00	0.01	0.01	0.01	0.00	0.01	0.00	0.00	0.00	0.00
Mg	0.00	0.00	0.00	0.00	0.06	0.04	0.01	0.03	0.04	0.02	0.02	0.02	0.00
Ca	0.00	0.00	0.00	0.00	0.00	0.00	0.00	0.00	0.00	0.00	0.00	0.00	0.00
V	0.00	0.00	0.00	0.00	0.00	0.00	0.00	0.00	0.00	0.00	0.00	0.00	0.00
Zn	0.00	0.00	0.00	0.00	0.00	0.00	0.00	0.00	0.00	0.00	0.00	0.00	0.18
X_{Hem}	0.06	0.07	0.03	0.00	0.07	0.08	0.04	0.02	0.15	0.69	0.67		
X_{Ilm}	0.94	0.93	0.97	1.00	0.88	0.88	0.94	0.95	0.81	0.28	0.30		

metasedimentary granofelses may suggest the onset of granulite facies conditions, typically estimated at >700 °C (e.g. Turner, 1981; Philpotts, 1990; Spear, 1993) or >800 °C according to Pattison *et al*. (2003). On the other hand, the absence of the assemblage orthopyroxene + sillimanite suggests that peak temperatures did not exceed 875 °C at ~10 kbar as constrained by the reaction:

$$\mathrm{Bt} + \mathrm{Grt} + \mathrm{Qtz} \rightarrow \mathrm{Opx} + \mathrm{Sill} + \mathrm{L}$$

calculated for the NaKFMASH system (Spear *et al*., 1999; reaction 7′, Fig. 7). For pressures, the absence of cordierite and presence of relict staurolite, kyanite and rutile suggest conditions in excess of 4–7 kbar at some stage during the history of these rocks (e.g. Thompson & Thompson, 1976; Holdaway & Lee, 1977; White *et al*., 2001).

Retrieval of peak *P–T* conditions in granulite facies metamorphic rocks using conventional thermobarometry (e.g. Fe–Mg exchange geothermometers between garnet, biotite, orthopyroxene, clinopyroxene and hornblende, or garnet–plagioclase–aluminosilicate–rutile–ilmenite, and Al in orthopyroxene geobarometers) seldom yields acceptable results, as re-equilibration through exchange and net transfer reactions during retrogression commonly obliterate peak compositions at such high temperatures (e.g. Spear & Peacock, 1989; Spear & Florence, 1992; Fitzsimons & Harley, 1994; Pattison & Bégin, 1994). In the case of the WSG rocks, almost all garnet shows evidence of resorption along the rims (e.g. Fig. 3b–d, 4a,b & 5e). Additionally, most pelitic/semipelitic samples are characterized by a high modal content of garnet relative to biotite, with both minerals almost always occurring in direct contact along rims in melanosomes. All these features suggest that garnet–biotite thermometry will not record peak temperatures (e.g. Spear & Peacock, 1989). Nonetheless, conventional thermobarometry using the intersections of Fe–Mg exchange garnet–biotite thermometer of Hodges & Spear (1982) with the garnet–rutile–ilmenite–plagioclase–quartz (GRIPS) barometer of Bohlen & Liotta (1986) was attempted on five samples (three pelitic/semipelitic schists and gneisses, a leucosome, and a pyroxene and hornblende-bearing garnet–biotite granofels). Calculations were done iteratively with the spreadsheet of Reche & Martinez (1996) on inclusions

Fig. 6. Selected textural relations in pelitic schists, leucosomes, granofelses and orthopyroxenites: (a) topotactic overgrowth of staurolite by kyanite, and their relation to sillimanite in the main foliation plane, sample WSG-2b, ppl; (b) prismatic sillimanite oriented in the main foliation plane (S_2), and overgrowing kyanite, sample WSG-2b, ppl; (c) fibrolite ($Sill_1$) replacing kyanite along the rim in leucosome, sample WSG-35, ppl; (d) staurolite included in garnet, sample WSG-2b, ppl; (e) BSEI showing the complex textural relations between magnetite, titan-hematite with exsolution lamellae of ilmenite, and matrix ilmenite, coexisting with plagioclase (black), sample WSG-14; (f) inclusions of rutile and fibrolite ($Sill_1$) in coarse-grained garnet; sample WSG-2b, ppl; (g) inclusions of quartz and biotite in orthopyroxene, sample WSG-23, ppl; (h) hypersthene (Opx) and subcalcic clinopyroxene (Cpx) coexisting with biotite, plagioclase and ilmenite (black), sample WSG-21, ppl. Note the partial replacement of the Cpx by anthophyllite and ankerite.

Table 6. Representative amphibole analyses.

	WSG-41				WSG-21								WSG-23			
	20 Hb	25 Hb	35 Hb	40 Hb	10 Hb	12 Hb	14 Hb	94 Hb	5 Anth	19 Anth	25 Anth	65 incl	41 Anth	2 Anth	3 Anth	4 Anth
SiO_2	40.60	41.92	40.97	46.67	43.16	42.54	41.82	45.54	53.94	54.55	53.56	55.61	55.70	55.84	55.37	55.54
TiO_2	0.15	0.26	0.66	0.61	0.37	0.24	0.20	0.64	0.00	0.04	0.04	0.00	0.06	0.10	0.01	0.02
Al_2O_3	15.44	15.32	15.48	10.18	14.52	15.19	15.07	11.42	2.70	2.56	3.34	2.03	2.01	1.82	1.68	1.64
Cr_2O_3	0.19	0.17	0.15	0.22	0.18	0.19	0.21	0.23	0.09	0.05	0.14	0.03	0.25	0.12	0.07	0.09
FeO	16.39	17.99	16.76	13.77	13.58	13.67	14.39	13.63	20.79	20.50	22.79	18.83	17.17	16.99	16.89	16.89
MnO	0.12	0.02	0.10	0.00	0.08	0.13	0.00	0.07	0.43	0.39	0.38	0.23	0.36	0.29	0.31	0.32
MgO	9.90	9.40	9.38	14.35	11.95	11.80	11.07	13.79	19.24	19.69	18.21	21.10	22.53	22.83	22.59	22.73
CaO	10.90	11.41	11.53	10.81	11.39	11.31	11.32	10.50	0.24	0.66	0.11	0.30	0.17	0.12	0.24	0.18
Na_2O	1.78	1.57	1.75	1.37	1.61	1.75	1.82	1.78	0.00	0.00	0.00	0.00	0.60	0.72	0.59	0.71
K_2O	0.48	0.32	0.36	0.13	0.42	0.64	0.51	0.20	0.00	0.00	0.00	0.00	0.00	0.00	0.00	0.00
Total	95.95	98.38	97.14	98.11	97.26	97.46	96.41	97.80	97.43	98.44	98.57	98.13	98.85	98.83	97.75	98.12
Si	6.02	6.10	6.06	6.58	6.24	6.15	6.15	6.46	7.79	7.78	7.70	7.89	7.83	7.85	7.86	7.86
Al^{iv}	1.98	1.90	1.94	1.42	1.76	1.85	1.85	1.54	0.21	0.22	0.30	0.11	0.17	0.16	0.14	0.14
Al^{vi}	0.72	0.72	0.76	0.27	0.71	0.74	0.76	0.37	0.25	0.21	0.27	0.23	0.16	0.15	0.14	0.13
Cr	0.02	0.02	0.02	0.03	0.02	0.02	0.02	0.03	0.01	0.01	0.02	0.00	0.03	0.01	0.01	0.01
Fe^{3+}	1.13	1.05	0.80	1.33	0.89	0.92	0.85	1.30	0.00	0.00	0.00	0.00	0.00	0.00	0.00	0.00
Ti^{iv}	0.02	0.03	0.07	0.07	0.04	0.03	0.02	0.07	0.00	0.00	0.00	0.00	0.01	0.01	0.00	0.00
Mg	2.19	2.04	2.07	3.02	2.57	2.54	2.43	2.91	4.14	4.19	3.90	4.46	4.72	4.78	4.78	4.79
Fe^{2+}	0.90	1.14	1.27	0.29	0.75	0.73	0.92	0.32	0.60	0.59	0.81	0.31	0.09	0.05	0.08	0.06
Mn	0.02	0.00	0.01	0.00	0.01	0.02	0.00	0.01	0.00	0.00	0.00	0.00	0.00	0.00	0.00	0.00
M1–3	5.00	5.00	5.00	5.00	5.00	5.00	5.00	5.00	5.00	5.00	5.00	5.00	5.00	5.00	5.00	5.00
Mg	0.00	0.00	0.00	0.00	0.00	0.00	0.00	0.00	0.00	0.00	0.00	0.00	0.00	0.00	0.00	0.00
Fe^{2+}	0.00	0.00	0.00	0.00	0.00	0.00	0.00	0.00	1.91	1.85	1.94	1.93	1.93	1.95	1.93	1.93
Mn	0.00	0.00	0.00	0.00	0.00	0.00	0.00	0.00	0.05	0.05	0.05	0.03	0.04	0.04	0.04	0.04
Ca	1.73	1.78	1.83	1.63	1.76	1.75	1.78	1.60	0.04	0.10	0.02	0.05	0.03	0.02	0.04	0.03
Na	0.27	0.22	0.17	0.37	0.24	0.25	0.22	0.41	0.00	0.00	0.00	0.00	0.00	0.00	0.00	0.00
Sum M4	2.00	2.00	2.00	2.00	2.00	2.00	2.00	2.00	2.00	2.00	2.00	2.00	2.00	2.00	2.00	2.00
Na	0.24	0.22	0.33	0.01	0.22	0.24	0.30	0.09	0.32	0.35	0.33	0.33	0.16	0.20	0.16	0.20
K	0.09	0.06	0.07	0.02	0.08	0.12	0.10	0.04	0.00	0.00	0.00	0.00	0.00	0.00	0.00	0.00
Sum A	0.34	0.28	0.40	0.03	0.29	0.36	0.40	0.12	0.32	0.35	0.33	0.33	0.16	0.20	0.16	0.20
Cations	15.34	15.28	15.40	15.03	15.29	15.36	15.40	15.12	15.32	15.35	15.33	15.33	15.16	15.20	15.16	15.20
X_{Mg}	0.71	0.64	0.62	0.91	0.77	0.78	0.72	0.90	0.62	0.63	0.59	0.67	0.70	0.71	0.70	0.71

of biotite in garnet, core pairs of matrix crystals, matrix rim pairs separated by plagioclase or quartz, and rim pairs of matrix crystals in contact (Appendix S2). The rationale behind such attempts was not to accurately determine peak *P–T* conditions inasmuch as to identify any trends of increasing or decreasing pressures and temperatures during garnet growth. The results, listed in Table 8, show that core pairs and inclusions typically yield higher pressures and temperatures compared with rim pairs, although no systematic change in *P–T* conditions is recorded for the same garnet crystal using biotite inclusions. Table 8 also shows that this iterative method yields a very wide range of temperatures and pressures (520–860 °C, 5.4–9.7 kbar) with most results being considerably lower than expected for these rocks. Application of the same method after arbitrarily assuming that 10% of the total Fe in biotite is Fe^{3+} yields *P–T* conditions that are 50–60 °C and 0.5–0.7 kbar lower than calculations that assume all Fe as Fe^{2+}.

Pattison *et al.* (2003) proposed a method for retrieving peak pressures and temperatures in granulite facies rocks by iteratively adjusting the Fe–Mg ratios of coexisting garnet and orthopyroxene until a unique *P–T* point of intersection between three independent equilibria among garnet, orthopyroxene and plagioclase is obtained. Application of this technique to the orthopyroxene-bearing sample WSG-21 (using program RCLC; Pattison *et al.*, 2003; an average orthopyroxene composition, and a model of octahedral Al; Table 7, and ignoring the presence of hornblende and subcalcic clinopyroxene) yielded a convergence point of 897 °C and 9.62 kbar. These conditions are considerably higher than a pressure of 7.5 kbar calculated using the Al in orthopyroxene barometer of Harley (1984) at an arbitrary temperature of 850 °C, and are slightly higher than indicated by phase relations (e.g. absence of Opx + Sill in metapelites; see above).

Application of the multiequilibrium approach to thermobarometry (e.g. Berman, 1991; Powell & Holland, 1994) using an internally consistent thermodynamic data base to each sample studied can be useful in constraining an average *P–T* condition per sample and identifying the extent of post-peak re-equilibration of the different lithologies. Moreover, iterative application of the Powell & Holland (1994) method of 'average *P–T* calculations' using THERMOCALC 3.26 (Powell & Holland, 2002) to the same sample by selectively eliminating end-members associated with large activity residuals normalized to

Table 7. Representative pyroxene analyses.

	WSG-21											WSG-23		
	1 Opx	4 Opx	7 Opx	8 Opx	Average*	Stdev*	14 Cpx	16 Cpx	20 Cpx	24 Cpx	91 Cpx	36 Opx	10 Opx	16 Opx
SiO_2	49.91	50.43	50.37	50.36	50.56	0.44	52.70	51.69	53.17	53.24	53.95	52.10	52.82	52.26
TiO_2	0.07	0.14	0.19	0.13	0.16	0.14	0.26	0.44	0.27	0.20	0.20	0.04	0.00	0.04
Al_2O_3	4.27	4.10	4.18	3.45	4.00	0.24	5.82	7.25	5.27	5.41	3.76	1.85	0.18	0.20
Cr_2O_3	0.05	0.08	0.09	0.10	0.09	0.02	0.19	0.22	0.19	0.23	0.05	0.13	0.18	0.22
Fe_2O_3	0.00	0.00	0.00	0.00	0.00	0.00	0.00	0.00	0.00	0.00	0.00	3.78	3.38	4.17
FeO	25.67	26.06	25.63	25.54	25.82	0.37	16.46	15.62	16.71	16.87	18.59	15.93	15.83	15.52
MnO	0.46	0.42	0.37	0.32	0.41	0.05	0.17	0.18	0.26	0.25	0.20	0.30	0.29	0.36
MgO	19.22	19.09	19.39	19.42	19.55	0.32	18.43	17.74	18.39	18.88	19.77	23.94	24.72	24.30
CaO	0.19	0.22	0.26	0.28	0.23	0.09	3.87	4.78	3.37	3.32	2.14	0.14	0.04	0.10
Na_2O	0.00	0.00	0.00	0.00	0.00	0.00	1.24	1.35	1.37	1.28	1.29	0.70	0.63	0.69
Total	99.84	100.54	100.48	99.60	100.82	0.82	99.14	99.28	99.01	99.68	99.95	98.91	98.07	97.86
Si^{iv}	1.89	1.90	1.90	1.91	1.90	0.01	1.94	1.90	1.96	1.95	1.98	1.93	1.97	1.96
Al^{iv}	0.11	0.10	0.10	0.09	0.10	0.01	0.06	0.10	0.04	0.05	0.02	0.07	0.01	0.01
T site	2.00	2.00	2.00	2.00	2.00	0.00	2.00	2.00	2.00	2.00	2.00	2.00	1.98	1.97
Al^{vi}	0.08	0.08	0.08	0.07	0.07	0.01	0.19	0.21	0.19	0.18	0.14	0.01	0.00	0.00
Ti	0.00	0.00	0.01	0.00	0.00	0.00	0.01	0.01	0.01	0.01	0.01	0.00	0.00	0.00
Cr	0.00	0.00	0.00	0.00	0.00	0.00	0.01	0.01	0.01	0.01	0.00	0.00	0.01	0.01
Fe^{+3}	0.00	0.00	0.00	0.00	0.00	0.00	0.00	0.00	0.00	0.00	0.00	0.11	0.09	0.12
Fe^{+2}	0.81	0.82	0.81	0.81	0.81	0.01	0.51	0.48	0.51	0.52	0.57	0.49	0.49	0.49
Mn^{+2}	0.01	0.01	0.01	0.01	0.01	0.00	0.01	0.01	0.01	0.01	0.01	0.01	0.01	0.01
Mg	1.09	1.07	1.09	1.10	1.09	0.01	1.01	0.97	1.01	1.03	1.08	1.32	1.37	1.36
Ca	0.01	0.01	0.01	0.01	0.01	0.00	0.15	0.19	0.13	0.13	0.08	0.01	0.00	0.00
Na	0.00	0.00	0.00	0.00	0.00	0.00	0.09	0.10	0.10	0.09	0.09	0.05	0.05	0.05
M_1,M_2	2.01	2.00	2.01	2.01	2.01	0.00	1.97	1.98	1.97	1.97	1.98	2.00	2.02	2.03
$X_{(Jd+Ac)}$	0.00	0.00	0.00	0.00	0.00	0.00	0.09	0.10	0.10	0.09	0.09	0.05	0.05	0.05
$X_{(R2TiAl2O6)}$	0.00	0.00	0.01	0.00	0.00	0.00	0.01	0.01	0.01	0.01	0.00	0.00	0.00	0.00
$X_{(R2R3AlSiO6)}$	0.08	0.08	0.08	0.07	0.07	0.01	0.06	0.10	0.04	0.05	0.02	0.07	0.01	0.01
X_{Wo}	0.01	0.01	0.01	0.01	0.00	0.00	0.08	0.10	0.07	0.07	0.04	0.01	0.00	0.00
X_{En}	0.53	0.52	0.53	0.53	0.53	0.01	0.49	0.46	0.50	0.50	0.54	0.64	0.69	0.68
X_{Fs}	0.39	0.39	0.39	0.39	0.39	0.01	0.25	0.22	0.25	0.25	0.28	0.24	0.24	0.24

*Average composition used for thermobarometry following Pattison *et al.* (2003).

uncertainty on their measured activity (e^*_k parameter of Powell & Holland, 1994), each time reducing the number of independent reactions used until a better (tighter) fit is obtained, can constrain peak *P–T* conditions if properly interpreted. Because this method takes into account the errors in activity calculations, it allows for the assessment of the results obtained through the value of 'σ_{fit}' (a measure of the scatter in residuals of the enthalpies and activities normalized by their uncertainties), and therefore has the advantage of providing an error envelope for pressure and temperature.

In this study, all end-member activities for mineral pairs used in conventional thermobarometry (indicated above) were calculated using AXWIN (Holland & Powell, 2005), and the results were used to determine an 'average *P–T* condition' defined by the intersection of all independent reactions using THERMOCALC 3.26 (Powell & Holland, 2002). Iterations were carried out until an acceptable (low) value for 'σ_{fit}' was obtained. The results of these calculations (Table S1) show that

1 The semipelitic (quartzofeldspathic) gneisses and the garnet–biotite–hornblende granofelses (e.g. WSG-2 & WSG-41) yielded the most consistent results, typically with the lowest 'σ_{fit}' and standard deviations (Table S1).

2 Pairs of cores of garnet and matrix biotite crystals from WSG-2 and WSG-41 yielded average temperatures of 869 ± 28 °C and 832 ± 57 °C respectively. Corresponding pressures for both samples were 9 ± 1 kbar. Rim pairs of garnet and matrix biotite crystals separated by quartz and plagioclase from both samples yielded temperatures that are 50–60 °C lower than those obtained by their cores, but identical pressures. Similar results (832 ± 32 °C, 9.7 ± 0.8 kbar for cores and 774 ± 27 °C, 9.2 ± 0.7 kbar for rims) were obtained for assemblages in leucosomes (WSG-27b; Table S1).

3 The metapelitic sample WSG-14 and the more retrograded garnet–biotite gneiss (WSG-2b) yield considerably lower average pressures and temperatures for cores and rims (820 ± 45 °C, 7 ± 1 kbar, and 750 ± 75, 8.5 ± 2.5 kbar respectively) than those obtained for samples showing limited signs of retrogression. These samples also yielded the largest scatter in *P–T* conditions with 'σ_{fit}' values that fail the χ^2 test (Powell & Holland, 1994), even when the number of independent reactions was reduced through the elimination of end-members with largest uncertainties in activity (Table S1; Fig. 7).

4 Calculations in which inclusions of biotite, hornblende or plagioclase in garnet were used typically yielded temperatures similar to those obtained using garnet and biotite core analyses for the same sample. However, no systematic trends in calculated pressure or temperature were observed from cores to rims of

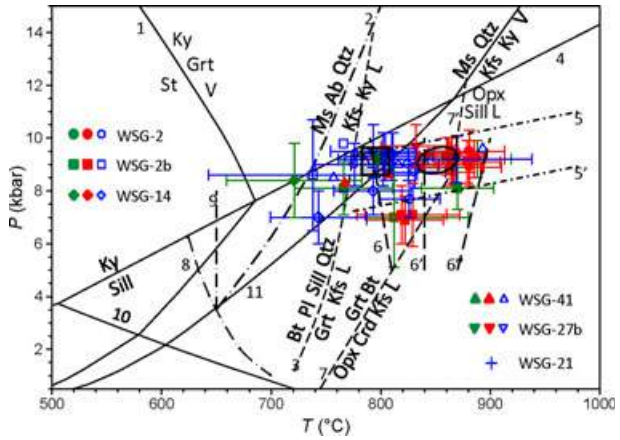

Fig. 7. *P–T* diagram showing the average *P–T* conditions for samples WSG-2, -2b, -14, -21, 27b and -41 calculated using THERMOCALC 3.26 (Powell & Holland, 2002) relative to some experimentally constrained or thermodynamically calculated pertinent equilibria. Filled solid black symbols: cores; open symbols: rims; grey symbols: biotite inclusions in garnet. Reactions 1, 4, 10 and 11 calculated using PTX (Perkins *et al.*, 1986) and the Berman (1991) Dec 06 database; large dash – dotted curves 2, 8 and 9, are from Thompson (2001); curve 3 represents biotite dehydration melting from Le Breton & Thompson (1988); short dash-dotted lines 5 and 5′ represent the reaction Rt + Grt = Ilm + Sill (Bohlen *et al.*, 1983), calculated for activities of minerals in WSG-2b using winTWQ (Berman, 2007); dashed line 6 represents the minimum solidus for metagreywackes; 6′ and 6″ represent the upper thermal stability of biotite during partial melting of metagreywackes with different Mg# (49 and 81, Stevens *et al.*, 1997); grey-dashed curve 7 and 7′ dehydration melting reactions of biotite (+Pl + Qtz) to produce Opx + Crd and Opx + Sill in the system NKFMASH respectively according to Spear *et al.* (1999). Shaded ellipse delineates preferred peak *P–T* estimates for WSG rocks calculated for core pairs of Grt and Bt, shaded square preferred *P–T* conditions for equilibration of Grt and Bt rims. Key: 1, Fe-St + Qtz = Ky/Sill + Alm + V; 2, Ms + Ab + Qtz + V = Ky + L; 3, Bt + Ky/Sill + Pl + Qtz = Grt + Ksp + L; 4, Ky = Sill; 5–5′, Rt + Grt = Ilm + Sill; 6–6′, Bt + Qtz + Pl_1 = Kfs ± Grt ± Crd + Opx + Pl_2 + L (X_{An} Pl_2 > X_{An} Pl_1); 7, Bt + Grt + Qtz = Crd + Opx + Kfs + L; 7′, Bt + Grt + Qtz = Opx + Sill + L; 8, Ms + Kfs + Ab + Qtz + V = L; 9, Ms + Ab + Qtz + V = Ky + L; 10, And = Sill.

the host garnet. Calculations using rims of garnet and biotite crystals in contact yielded conditions comparable to those obtained using rim pairs of crystals separated by quartz or feldspar, and do not necessarily provide better constraints on the *P–T* conditions of Fe–Mg exchange closure during retrogression.

5 For the garnet–biotite–hornblende granofels with two pyroxenes (WSG-21), the average *P–T* method failed to give reasonable estimates for all 16 independent reactions. However, after eliminating all amphibole and Mn-bearing end-members, and solving for an optimum pressure within a temperature range of 700–1000 °C using rim compositions, an average pressure of 9.2 ± 0.88 kbar was obtained from five independent reactions (Table S1). Solving for an optimum temperature at 9.2 kbar yielded 869 ± 69 °C with a σ_{fit} of 1.7 (Table S1).

6 Calculations carried out for the orthopyroxenites (e.g. WSG-23) yielded unreasonably low temperatures and pressures (350–500 °C, 4.4–7.7 kbar), which we reject.

The results of multiequilibrium calculations (Table S1), coupled with the phase relations discussed above (e.g. reactions 7 & 7′, Fig. 7), lead us to conclude that WSG rocks attained peak *P–T* conditions of 850 ± 30 °C, 9 ± 1 kbar. Near-isobaric cooling led to the re-equilibration of garnet, biotite ± plagioclase along their rims at 795 ± 58 °C. This was either accompanied with or followed by the occurrence of net transfer reactions involving garnet, feldspar, Fe-oxides, and melt, the effects of which are evidenced by textures developed in pelitic rocks (WSG-14 & WSG-2b). The fact that the *P–T* results obtained using RCLC and some calculations with THERMOCALC are ~0.5 kbar and 30–40 °C higher than the above estimates could be an artefact of assuming all Fe in biotite as Fe^{2+}. On the other hand, we consider the results obtained using THERMOCALC as generally being more satisfactory than those obtained using RCLC because the former method gives an error envelope based on uncertainties in calculated activities, and is therefore more 'forgiving' of errors in activities or actual analyses. Errors in activities of anorthite (potentially related to underestimation of the Na_2O content of plagioclase through EDS analysis) result in an over-estimation of pressure (and therefore corresponding temperature), and may explain the higher temperature obtained by RCLC.

MONAZITE CHEMISTRY AND AGES

Monazite is a useful mineral for dating amphibolite and granulite facies metamorphism, because it is nearly ubiquitous in pelitic rocks, commonly growing at temperatures close to those necessary for the crystallization of garnet, staurolite or one of the aluminosilicate polymorphs (e.g. Parrish, 1990; Smith & Barreiro, 1990; Kingsbury *et al.*, 1993; Wing *et al.*, 2003; Kohn & Malloy, 2004; Tomkins & Pattison, 2007). Monazite is also characterized by a high content of radiogenic Pb relative to that of common Pb, high closure temperatures (650–900 °C, depending on cooling rate and grain size; e.g. Cherniak & Watson, 2001; Cherniak *et al.*, 2004; Harrison *et al.*, 2002) making it highly retentive of Pb, and is resistant to Pb loss by thermally activated volume diffusion at temperatures below those of the first sillimanite-in isograd. Although monazite ages may be partially reset by fluid assisted dissolution and reprecipitation, the common preservation of several age domains within this mineral, and the ability to link their growth to specific metamorphic and anatectic events (e.g. Foster *et al.*, 2002; Pyle & Spear, 2003; Pyle *et al.*, 2005) has commonly led to significant tectonic interpretations.

Table 8. Results of thermobarometric calculations.

Grt #	Bt #	Texture	X_{Alm}	X_{Prp}	X_{Sps}	X_{Grs}	X_{Al}^{vi}	X_{Ti}	X_{Phl}	X_{Ann}	X_{Ab}	X_{An}	X_{Ilm}	$\ln K_D^{Gt\text{-}B}$	T (°C)[a]	P (kbar)[a]	T* (°C)[b]	P (kbar)[b]	TWQ[c]
WSG-2																			
8	9B	incl	0.71	0.21	0.02	0.07	0.09	0.09	0.45	0.35	0.64	0.36	0.95	1.50	703	8.3	659	7.7	677, 7.7
30	9B	incl	0.71	0.21	0.02	0.07	0.09	0.09	0.45	0.35	0.64	0.36	0.95	1.49	709	8.3	664	7.7	677, 7.7
31	1	incl	0.70	0.22	0.02	0.06	0.15	0.03	0.45	0.36	0.64	0.36	0.95	1.34	776	8.8	725	8.2	610, 5.8
27	3 core	cores	0.67	0.26	0.02	0.05	0.15	0.03	0.45	0.36	0.64	0.36	0.93	1.17	863	9.4	802	8.6	
core_5	sm_15	cores	0.74	0.18	0.02	0.07	0.15	0.03	0.45	0.37	0.64	0.36	0.94	1.63	649	7.6	610	7.1	
13_gtl_prof_c	sm_15	cores	0.67	0.25	0.02	0.06	0.15	0.03	0.45	0.37	0.64	0.36	0.94	1.18	861	9.7	802	9.0	
23	10	rims	0.74	0.16	0.02	0.07	0.13	0.04	0.44	0.38	0.64	0.36	0.93	1.69	633	7.7	595	7.1	616, 6.2
16	6	rims	0.72	0.19	0.02	0.07	0.14	0.03	0.46	0.36	0.64	0.36	0.93	1.55	685	8.2	642	7.6	642, 6.8
18	8	rims	0.70	0.21	0.02	0.07	0.14	0.03	0.45	0.37	0.64	0.36	0.93	1.44	732	8.6	685	7.9	650, 6.9
6_1	sm_12_c	cores	0.75	0.16	0.03	0.07	0.16	0.03	0.45	0.36	0.64	0.36	0.93	1.76	602	7.0	567	6.5	700, 8
8_6	sm_13	cores	0.73	0.18	0.02	0.07	0.16	0.03	0.44	0.36	0.64	0.36	0.93	1.61	659	7.7	618	7.2	630, 6.8
15	5b	rims;c	0.73	0.18	0.02	0.07	0.15	0.03	0.44	0.37	0.64	0.36	0.93	1.59	664	7.8	623	7.2	630, 6.9
WSG-2b																			
Gtl_Sp3_12	23	incl	0.78	0.13	0.02	0.07	0.09	0.03	0.45	0.43	0.59	0.41	1.00	1.80	587	6.5	552	6.1	620, 7
Gtl_Sp3_17	30	incl	0.75	0.19	0.02	0.04	0.10	0.03	0.54	0.32	0.59	0.41	1.00	1.92	534	4.9	503	4.5	550, 7
Gtl_Sp3_33	17	incl	0.79	0.15	0.02	0.05	0.08	0.03	0.44	0.45	0.59	0.41	1.00	1.64	633	6.3	489	4.2	630, 7.8
Gtl_Sp3_36	24	incl	0.74	0.20	0.02	0.04	0.10	0.03	0.57	0.30	0.59	0.41	1.00	1.96	519	4.6	594	5.9	560, 6.7
Gtl_Sp3_lc	4	incl	0.75	0.19	0.02	0.04	0.11	0.04	0.47	0.38	0.59	0.41	1.00	1.61	640	6.0	600	5.6	750, 7
Gtl_Sp3_l_c	27	cores	0.75	0.19	0.02	0.04	0.10	0.03	0.46	0.40	0.59	0.40	1.00	1.54	671	6.4	629	5.9	650, 6.3
Gt2_Sp5_lc	20	cores	0.76	0.18	0.02	0.04	0.16	0.03	0.45	0.36	0.58	0.42	1.00	1.65	627	5.9	600	5.6	520,4
Gt3_Sp5_lc	7	cores	0.73	0.21	0.02	0.05	0.09	0.04	0.49	0.36	0.58	0.42	1.00	1.56	661	6.2	620	5.7	650, 6.3
Gtl_Sp3_lc	11	cores	0.75	0.19	0.02	0.04	0.10	0.03	0.46	0.41	0.59	0.40	1.00	1.51	683	6.5	640	6.0	
Gt3_Sp5_9	6	rims	0.76	0.13	0.02	0.10	0.13	0.03	0.47	0.36	0.58	0.42	1.00	2.05	523	6.3	494	5.9	550, 6.1
Gt3_Sp5_8	7	rims	0.70	0.21	0.02	0.07	0.09	0.04	0.49	0.36	0.58	0.42	1.00	1.53	688	7.4	645	6.8	
Gt3_Sp5_8	6	rims	0.70	0.21	0.02	0.07	0.13	0.03	0.47	0.36	0.58	0.42	1.00	1.50	702	7.5	658	7.0	
Gt4_Spl_2	2	rims;c	0.75	0.13	0.02	0.10	0.10	0.03	0.48	0.38	0.58	0.42	1.00	2.00	539	6.5	509	6.1	700, 7
Gtl_Sp3_8	3	rims;c	0.75	0.19	0.02	0.04	0.10	0.04	0.46	0.40	0.58	0.42	1.00	1.54	667	6.1	625	5.7	580, 6
WSG-14																			
51	81	incl	0.69	0.18	0.08	0.05	0.12	0.05	0.51	0.31	0.64	0.34	0.99	1.82	573	6.2	539	5.8	600, 6
54	81	incl	0.69	0.19	0.07	0.04	0.12	0.05	0.51	0.31	0.64	0.34	0.99	1.75	591	6.2	555	5.7	600, 6
44	76	incl	0.70	0.17	0.09	0.05	0.10	0.05	0.50	0.34	0.64	0.34	0.99	1.79	579	6.2	545	5.8	600, 6
43	76	incl	0.69	0.18	0.08	0.05	0.10	0.05	0.50	0.34	0.64	0.34	0.99	1.73	601	6.5	564	6.0	610, 6.4
2	9	cores	0.65	0.19	0.11	0.05	0.10	0.06	0.44	0.40	0.59	0.41	1.00	1.30	783	7.2	731	6.6	706, 5.8
5	22	cores	0.68	0.17	0.11	0.05	0.10	0.05	0.46	0.37	0.59	0.41	1.00	1.57	656	5.8	615	5.3	650, 6
14	27	cores	0.68	0.18	0.10	0.04	0.10	0.06	0.46	0.38	0.59	0.41	1.00	1.54	670	5.9	628	5.5	640, 6
26	35	cores	0.68	0.17	0.11	0.04	0.09	0.06	0.45	0.39	0.64	0.35	1.00	1.52	679	6.4	636	5.9	650, 6.1
39	55	cores	0.67	0.18	0.11	0.04	0.08	0.06	0.44	0.41	0.64	0.34	1.00	1.41	728	6.7	681	6.2	700, 6.2
36	66	rims	0.67	0.16	0.12	0.04	0.07	0.07	0.44	0.41	0.69	0.30	1.00	1.49	694	6.8	649	6.2	680, 6.2
Gt_1	10	rims	0.66	0.19	0.10	0.05	0.11	0.05	0.44	0.39	0.64	0.35	1.00	1.34	764	7.5	714	6.9	693, 6.1
20	34	rims	0.67	0.16	0.12	0.05	0.10	0.05	0.45	0.39	0.64	0.35	1.00	1.60	646	6.1	606	5.6	640, 6
23	34	rims	0.68	0.16	0.12	0.05	0.13	0.03	0.47	0.36	0.64	0.35	1.00	1.74	594	5.4	584	5.3	630, 5.8
12	7	rims;c	0.66	0.17	0.12	0.04	0.11	0.06	0.44	0.39	0.59	0.41	1.00	1.47	697	6.1	653	5.6	680, 6
6	20	rims;c	0.67	0.16	0.12	0.05	0.11	0.05	0.47	0.37	0.64	0.35	1.00	1.66	623	5.8	585	5.3	630, 5.8
32	100	cores	0.67	0.16	0.12	0.05	0.10	0.06	0.45	0.39	0.59	0.41	1.00	1.55	665	5.9	623	5.4	650, 6
35	99	rims;c	0.67	0.15	0.13	0.04	0.10	0.05	0.44	0.41	0.69	0.30	1.00	1.54	669	6.5	627	6.0	700, 6
WSG-27b																			
18	11	cores	0.58	0.30	0.04	0.08	0.09	0.09	0.45	0.35	0.64	0.36	1.00	0.91	1039	7.8	1047	11.0	
9c	1	cores	0.65	0.21	0.06	0.08	0.15	0.03	0.45	0.36	0.64	0.36	1.00	1.31	799	9.1	701	7.7	
1	9B	rims	0.59	0.27	0.04	0.10	0.09	0.09	0.45	0.35	0.64	0.36	1.00	1.03	966	8.3	937	10.5	
10	10	rims	0.67	0.18	0.06	0.09	0.13	0.04	0.44	0.38	0.64	0.36	1.00	1.48	721	7.7	680	7.8	
WSG-41																			
1c	3	cores	0.57	0.23	0.03	0.17	0.07	0.04	0.47	0.42	0.45	0.55	0.99	1.02	1015	12.4	944	11.5	
9c	10	cores	0.56	0.26	0.02	0.16	0.09	0.04	0.48	0.38	0.45	0.55	0.99	1.01	1021	12.1	949	11.3	
27c	15	rims	0.56	0.25	0.02	0.17	0.09	0.04	0.45	0.41	0.45	0.55	0.99	0.90	1108	13.3	971	11.7	
14r	9	rims	0.56	0.27	0.02	0.15	0.09	0.04	0.47	0.40	0.45	0.55	0.99	0.90	1101	12.8	1019	11.9	
16r	11	rims	0.55	0.28	0.02	0.15	0.09	0.04	0.47	0.39	0.45	0.55	0.99	0.86	1132	13.1	1047	12.1	
19r	12	rims	0.56	0.26	0.02	0.16	0.08	0.04	0.47	0.41	0.45	0.55	0.99	0.89	1106	13.1	1025	12.2	
25r	17	rims	0.57	0.24	0.02	0.16	0.08	0.04	0.48	0.41	0.45	0.55	0.99	1.02	1008	12.1	938	11.2	
21r	6	rims	0.57	0.22	0.03	0.19	0.08	0.04	0.46	0.41	0.45	0.55	0.99	1.10	973	12.1	907	11.3	
28r	17	rims	0.59	0.23	0.02	0.15	0.08	0.04	0.48	0.41	0.45	0.55	0.99	1.13	937	11.3	874	10.6	
36r	17	rims	0.57	0.26	0.02	0.15	0.08	0.04	0.48	0.41	0.45	0.55	0.99	0.96	1053	12.4	978	11.5	
Gt_2	2	rims;c	0.57	0.23	0.03	0.18	0.09	0.04	0.47	0.40	0.45	0.55	0.99	1.08	976	12.0	910	11.1	

Incl, inclusions in garnet; rims;c, rims in contact.
[a] P and T conditions constrained by iterative solution of Grt–Bt thermometer of Hodges & Spear (1982) and GRIPS (Bohlen & Liotta, 1986), calculated using GPT3 (Reche & Martinez, 1996).
[b] P–T conditions calculated as in (a) assuming Fe^{3+} in Bt = 10% total Fe_{Bt}.
[c] P–T estimates obtained using WinTWQ (v. 2.34) (Berman, 2007).

In this study, U–Th–Pb dates are presented for eight monazite crystals in one pelitic schist (WSG-14), in an attempt to provide more detailed constraints on the P–T–t history of this area. This sample was selected because of (i) the relative abundance of monazite crystals occurring in a variety of different textural

relations; and (ii) its pelitic composition, which makes it more amenable for the dissolution and reprecipitation of overgrowths on accessory minerals (e.g. Spear & Kohn, 1996; Foster *et al.*, 2000; Rubatto *et al.*, 2001; Spear & Pyle, 2002; Hermann & Rubatto, 2003; Pyle & Spear, 2003; Gibson *et al.*, 2004) and therefore most likely to record most of the effects of the various metamorphic, anatectic, and hydrothermal events that may have affected this area.

Zoning patterns in monazite

The eight crystals analysed in this study range in size from 14 to 170 μm, and in textural context from inclusions in garnet and plagioclase to elongated crystals in the matrix (Fig. 8). BSE images and WDS X-ray intensity maps for Y, U, Th and Ca for all eight monazite crystals show that they are complexly zoned, with inclusions in garnet displaying a concentric or intergrowth pattern, and all matrix crystals characterized by 'patchy' patterns, following the terminology of Zhu & O'Nions (1999). For most crystals, the X-ray maps show that the concentration of Y is positively correlated with that of U, and negatively correlated with Th (Figs S2a, S3a, S4a, S5a,d and S6a), a pattern common to many monazite crystals (e.g. Spear & Pyle, 2002).

The yttrium X-ray maps best display the zoning in all monazite crystals, typically showing distinct patterns with sharp, well-defined outlines. Because Y variation is believed to record a history of monazite growth in many cases (e.g. Spear & Pyle, 2002; Gibson *et al.*, 2004), we have relied primarily on the concentration of this element to identify four distinct chemical zones in monazite crystals from WSG-14 (Figs S2–S6). The other criterion used to identify these zones is their

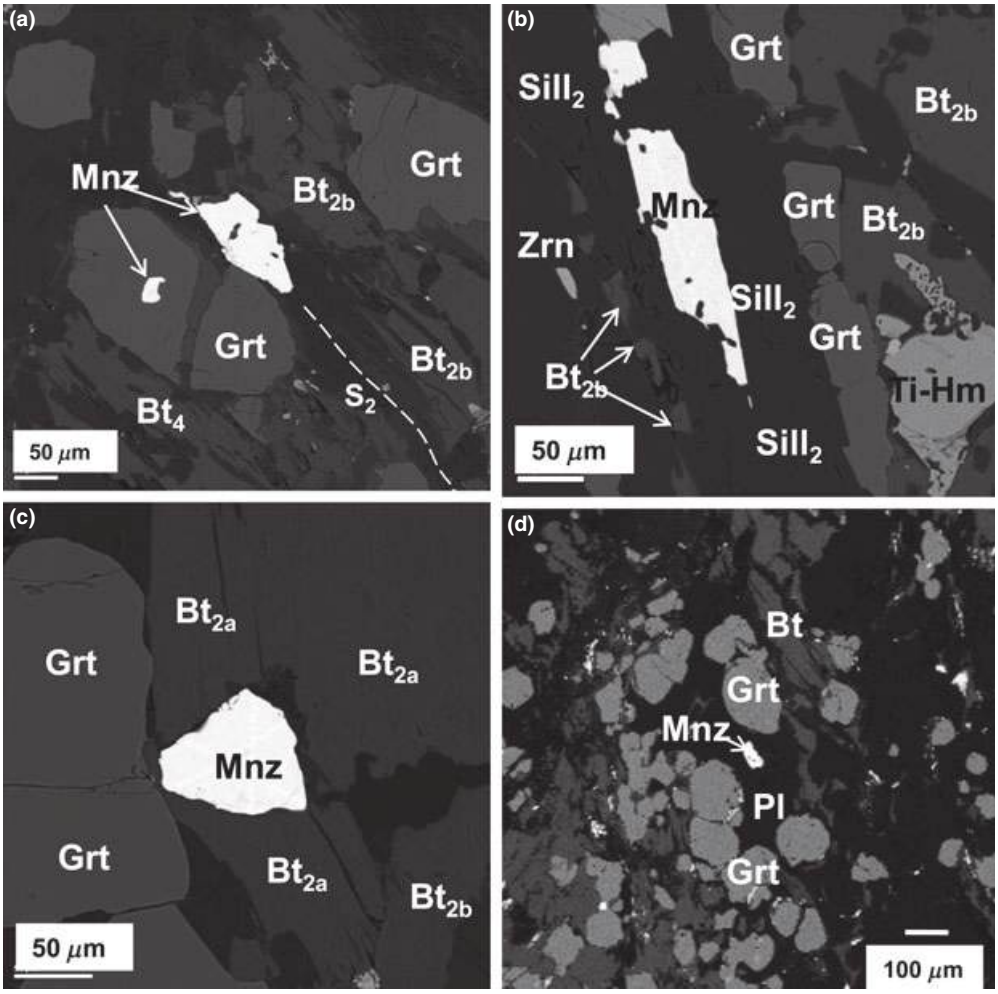

Fig. 8. Back-scattered electron images showing textural relations for five of the eight monazite crystals dated from sample WSG-14. (a) Cusp-shaped monazite inclusion in garnet (Sp1 Mnz1) next to a matrix monazite crystal elongated in the foliation plane (Mnz 7); (b) elongated monazite crystal (Mnz 10) oriented in the main foliation (S_2) defined by $Sill_2$ and Bt_{2b}; (c) monazite crystal (Mnz 6) shielded by biotite and garnet. Dark thin selvage separating monazite from some biotite consists of quartz and muscovite; (d) monazite inclusion in plagioclase (Mnz 8).

Th/U ratios (Fig. 9a,b), which may help constrain monazite growth in equilibrium with melts or hydrothermal fluids (e.g. Rubatto *et al.*, 2001; Pyle *et al.*, 2005). According to this scheme, zone 1 is characterized by the highest Y contents (Y > 10,000 ppm), a Th/U typically <25, and usually occurs as minute irregular patches close to the centres of many grains. Zone 2 is characterized by Y = 5000–10,000 ppm and Th/U < 25, and is common to most crystals, typically forming the bulk of their interior portions. Zone 3, which is dark on Y maps and is ubiquitous in all matrix monazite, is characterized by Y < 5000 ppm

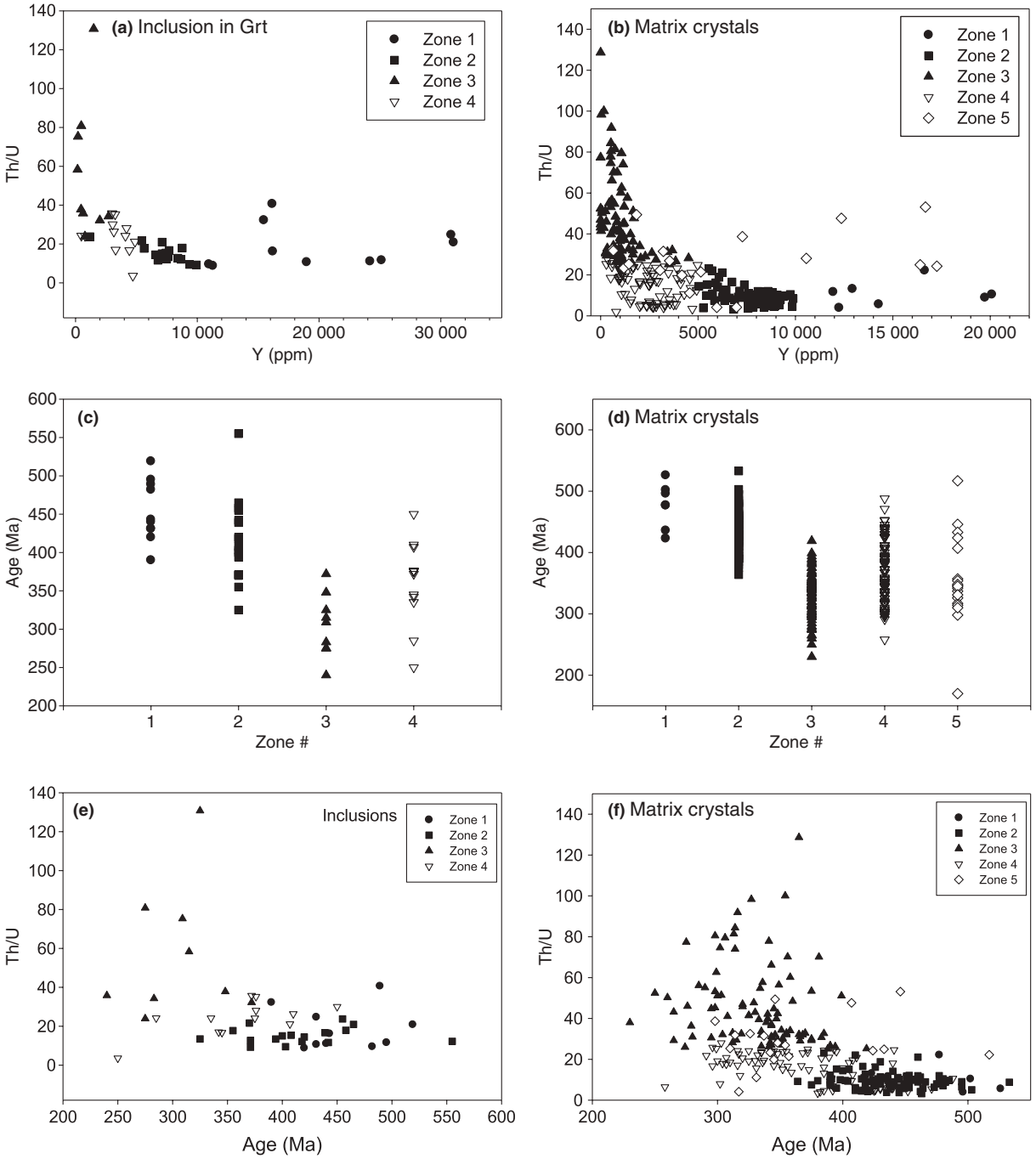

Fig. 9. Chemical and geochronological differences between the compositional zones observed in the dated monazite crystals. (a) and (b) Th/U *v.* Y plots for monazite inclusions in garnet (a) and matrix crystals (b); (c) and (d) chemical ages for the compositional zones for inclusions in garnet (c) and matrix monazite (d); (e) and (f) Th/U *v.* age for different zones in (e) inclusions and (f) matrix crystals.

(typically a few hundreds of ppm), and Th/U values >25. Zone 4 has Y values of 0–5000 ppm, Th/U typically <25, and occurs as diffuse areas in various parts of many crystals. In addition to these four zones, many matrix crystals have very thin, Y-rich (typically >5000 ppm) discontinuous rims with variable Th/U, which we describe as zone 5 (e.g. Figs S3b & S6b). Very few crystals display all five compositional zones. Whereas zone 1 is well developed in monazite inclusions in garnet, plots of Th/U *v.* Y show that most matrix monazite consists of zones 2 and 3 (Fig. 9). Figure 9 also shows that zones 4 and 5 are characterized by large variations in calculated dates.

Monazite U–Th–Pb ages

A U–Pb–Th 'age' (herein termed 'date') was calculated for each monazite analysis following the 'top-down' technique described above (cf. analytical techniques and Loehn, 2009). Typical uncertainties on individual spot analyses range from ±25 to ±100 Myr (2σ), calculated from propagating 2σ uncertainties in elemental concentrations through the chemical dating equation of Montel *et al.* (1996) using the EPMA dating Excel™ add-in (Pommier *et al.*, 2003). The resulting calculated dates were plotted on BSE images (e.g. Fig. S2), and presented as profiles along their respective traverses (Figs S3–S6).

Data were compiled in an Excel™ template worksheet automatically generated by the add-in program EPMA (Pommier *et al.*, 2003), and sorted by apparent age, in descending order. This sorting allowed for quick identification of outliers at each extreme of the data range, which could then be eliminated with sufficient justification (i.e. in-crack analysis, off-grain analysis, etc.). Calculated 'Age Error' was used to determine which analyses needed closer evaluation (i.e. based on an unusually high error), and all analyses with an age error >15% were excluded from final age analysis and histograms/probability density plots/or weighted mean age calculations of Figs S2–S6 (cf. Appendix S3). After the data were sorted based on apparent age, several plots were generated with ISOPLOT3 (Ludwig, 2003). Weighted-average age plots were then generated from the initially selected age groupings, which yielded information about probability of fit and MSWD (McIntyre *et al.*, 1966; Wendt & Carl, 1991). The probability of fit defines how well the individual spot-dates in the group correlate with each other, and the MSWD indicates the degree to which the scatter in ages can be accounted for by the uncertainties on the individual dates. Accordingly, a well-defined age population should have both a probability of fit and an MSWD close to 1.0.

Most monazite crystals are dominated by two distinct weighted average age populations at *c.* 440 and 360 Ma that show significant correlation with chemical zones 2 and 3 respectively. A third age population of 533–480 Ma is defined mostly by irregular islands close to the cores of the monazite crystals and corresponds to the Y-rich zone 1 (Fig. 9a–d). Analyses yielding relatively young dates are more commonly observed towards the grain exteriors. Although inclusions in garnet and matrix monazite show similar age populations and trends, a few monazite crystals included in garnet are generally characterized by a larger areal percentage of the older age population (>480 Ma; constituting 10% of all monazite inclusion dates; Fig. S2). One monazite (Sp1Mnz1) included in a garnet with relatively few fractures (Fig. 8; Fig. S2a,b) yields only two weighted average age populations of 445 ± 18 Ma (MSWD = 0.28; probability = 0.92), and 505 ± 36 Ma (MSWD = 0.41; probability = 0.52; Fig. S2c). These results attest to the somewhat limited ability of garnet to protect monazite inclusions from late stage events, given its tendency to develop fractures and microfractures (e.g. Foster *et al.*, 2000; Montel *et al.*, 2000) that could constitute pathways for fluids into the garnet interiors (Hames & Menard, 1993).

Matrix crystals that are partly surrounded by coarse-grained biotite or that occur in garnet pressure shadows (e.g. Mnz 6; Figs. 8 & S3) can have up to five well-defined chemical zones. These crystals yield up to three distinct age populations of *c.* 350, 450 and 490 Ma respectively (e.g. Fig. S3g). Matrix monazite surrounded by plagioclase, and which displays the most complex patchy zoning patterns with highly irregular and sometimes diffuse boundaries, also yield two age populations (*c.* 420 and ≤360 Ma) with few dates >480 Ma (e.g. Fig. S5). Conversely, some of the matrix monazite that is elongated in the main foliation plane S_2 and are chemically nearly homogeneous (e.g. Mnz 7; Fig. 8b; Fig. S6) are characterized by age histograms with a single mode and weighted mean age of 346 ± 13 Ma (Fig. S6e–g).

A probability density plot for all dates with <15% error obtained on all monazite crystals shows a continuum with no clear breaks to define subpopulations, and with a mean of 404 ± 54 Ma (Fig. 10a). However, these data are characterized by an MSWD of 5.6, and a probability of fit = 0, which, for a data set containing more than 250 points, indicates that this average 'age' is meaningless, and that the data represent a mixture of several age populations. On the other hand, Fig. 10a shows two broad, ill-defined peaks at *c.* 360–340 and 460–400 Ma, and a minor tail at 540–480 Ma. Calculation of a mean age weighted by data point errors for each of these three populations yields 509 ± 14, 438 ± 4.5 and 360.4 ± 5 Ma (2σ errors) for 5%, 51% and 44% of all data respectively, and acceptable MSWD and probabilities of fit (Fig. 10). Although the correspondence between the chemical zones and these three age populations is not always perfect, there is a clear decrease in age from zones 1 through 3 (Fig. 9). This is also supported by calculations of a simple mean and standard deviation for dates obtained for each chemical zone which yield

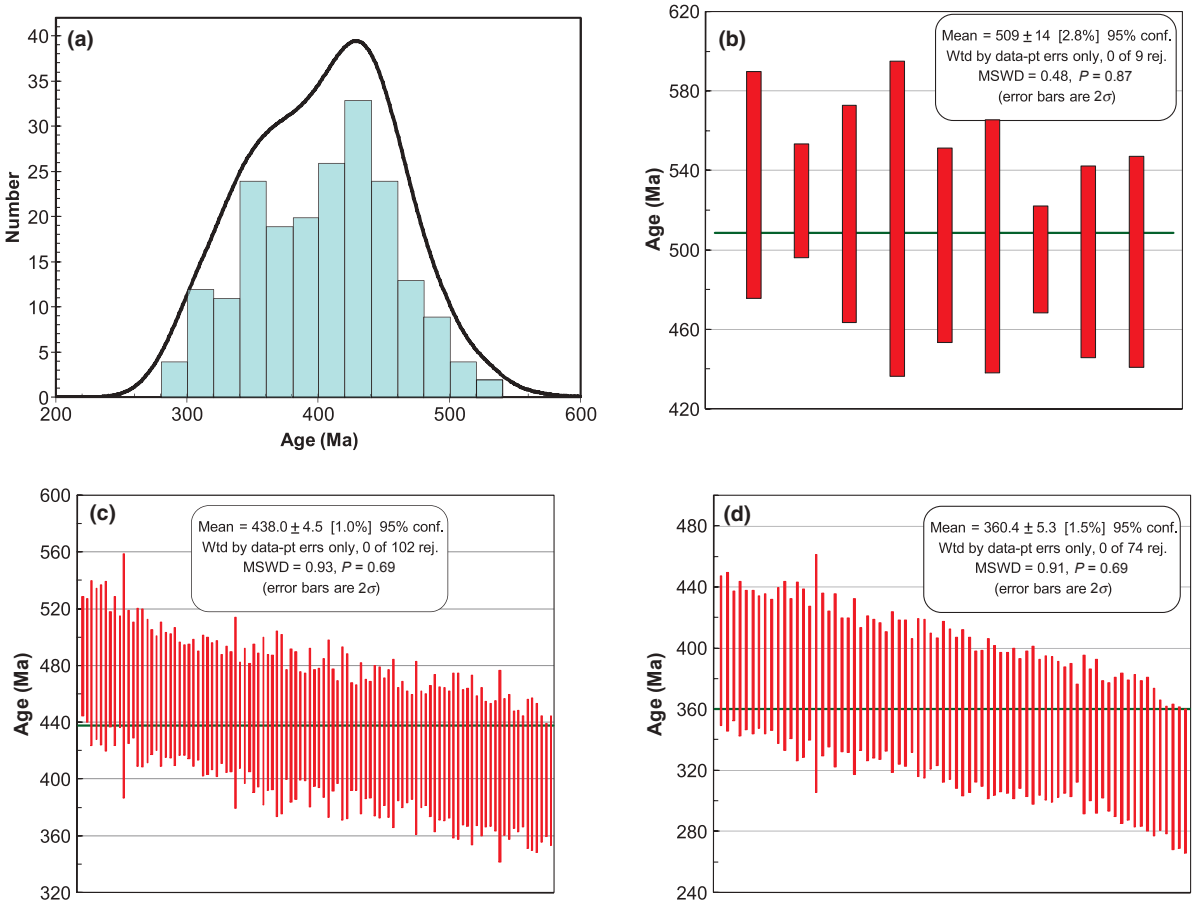

Fig. 10. (a) Probability density plot (ISOPLOT v. 3.0, Ludwig, 2003) for all ages obtained on all monazite crystals with errors $<15\%$. Weighted mean ages, 2σ errors, MSWD and probability calculated for each of the three age populations at 509, 438 and 360 Ma are shown in (b) (c) and (d).

470 ± 35, 434 ± 34 and 351 ± 29 Ma, for zones 1, 2 and 3 respectively. These results lead us to the conclusion that monazite crystals record episodes of growth at *c*. 500, 438 and 360 Ma.

The irregular outlines of chemical zones 1 and 2 suggest that monazite was partly resorbed/dissolved following each of the episodes of growth at *c*. 500 and 438 Ma. Zone 4 represents values intermediate between zones 2 and 3 for Y, Th/U, as well as calculated dates (simple mean of 382 ± 50 Ma). We therefore interpret this zone to have formed over an interval when zone 2 monazite was being dissolved and zone 3 precipitated episodically, making its dates 'mixed' and hence geologically meaningless. Outermost discontinuous rims representing zone 5 are volumetrically minor and subject to analytical uncertainties related to edge effects; thus we do not consider their associated 'dates' meaningful, although their high Y values suggest development at a time when a Y-rich phase (e.g. garnet or xenotime) was partly being consumed. It is therefore concluded that monazite growth and dissolution were for the most part episodic, and can be tentatively correlated with the reaction, deformational and anatectic history of the rocks as shown in Fig. 11.

P–T–t evolution

The *P–T–t* history of the WSG rocks can be summarized in a number of stages based on the textural, mineral chemical, thermobarometric, and geochronological data presented above. The occurrence of staurolite as inclusions in garnet (Fig. 6d) and as crystals overgrown topotactically by kyanite (Fig. 6a) indicates that garnet and kyanite crystallized in pelitic rocks at the expense of staurolite at >4 kbar and >650 °C according to the reaction (Spear & Cheyney, 1989):

$$\mathrm{St} + \mathrm{Ms} \rightarrow \mathrm{Grt} + \mathrm{Ky}_1 + \mathrm{Bt}_2 + \mathrm{H_2O}. \qquad (1)$$

The occurrence of zinc-bearing 'hercynite' (Table 5) in a few samples is probably due to the breakdown of any remaining staurolite according to a reaction similar to: staurolite → hercynite + kyanite + vapour. Although highly conjectural, the earliest monazite zone 1 (*c*. 500 Ma) may have crystallized before or during this stage (as the onset of monazite crystalli-

Mnz zone	1		2		3		5
Age (Ma)	> 500?		*c.* 450 – 430		370 – 350	300 – 270?	< 270?
			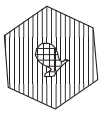		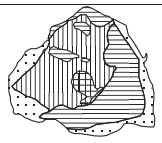	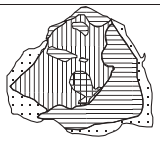	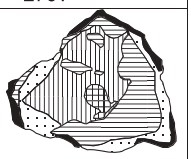
Stable minerals	Bt_1 + Bt_2 + Grt + St	Grt, Bt_2, Ky_1		Bt_2, $Sill_2$	Grt + Bt_2 + $Sill_3$ Ilm + Mgt + Ti-Hm		Bt_3, Chl, Cc, Ank
Melt/ fluid	-	-	Generated	Rapidly extracted	Hydrothermal fluid		Fluid-aided retrogression
Reactions		St + Ms ⇔ Grt + Bt_{2a}+ Ky1 *(Mnz resorbed as subsolidus Grt grows)*	1) Ms + Ab + Qtz ⇔Kfs + Ky_2 + L 2) Bt_{2a} + Ky + Qtz ⇔Grt + Kfs + L 3) Ky ⇔ $Sill_1$ 4) Bt_{2a} + $Sill_1$ ⇔ Grt + Kfs + L *(Grt overgrows Sill)*	*(Grt resorbed; Mnz resorbed?)* Grt + Kfs + L → Bt_{2b} + $Sill_2$ *($Sill_2$ along Grt rims)* L + Kfs + H_2O → Ms	Bt_2 + $Sill_2$ ⇔ Grt + Kfs + L Fibrolite along plagioclase grain boundaries *(Mnz grows in presence of fluid; hence its high Th/U)*	Limited Grt resorption; *(Allanite crystallizes retrogressively as Grt is resorbed)* Mylonitization?	Bt → Chl Grt → Chl *(Mnz outermost rims grow in presence of fluid as Grt dissolves)*
T (°C)		650→700	750 → 870	870 → 700	700 → 750	750 → 650	< 650
P (kbar)	> 4		9 → 11	9 → 8	7	7 → 6	< 6
Deformation	?	D_1	D_2	D_2	D_2	D_3	D_4
Schistosity	?	S_1	S_2	S_2	S_2		

Fig. 11. Stages of evolution of the Winding Stair Gap rocks related to the chemical (growth?) zones observed in monazite, different metamorphic mineral assemblages observed in pelitic schists, quartzofeldspathic gneisses, granofelses and leucosomes, calculated *P–T* conditions, melt generation and extraction, and deformational history.

zation in many metapelites commonly coincides with the staurolite–in isograd or the first appearance of one of the aluminosilicates; Smith & Barreiro, 1990; Wing *et al.*, 2003). We also suggest that most of the biotite inclusions in garnet (Bt_1) represent crystals that formed with or before staurolite, and were later trapped during the growth of garnet by continuous reaction (1). As garnet and biotite (Bt_2) continued to grow according to reaction (1), monazite zone 1 underwent localized dissolution/reprecipitation, hence accounting for the highly irregular outline of these 'relict islands'. Deformation accompanying this stage may have resulted in the shearing and reorientation of biotite (Bt_{2a}) into mica fish, followed by a second reorientation of some crystals to produce the S_1 foliation defined by Bt_{2b} and Ky_1 (Fig. 5b,c).

The occurrence of fine-grained, rounded, inclusion-free crystals of garnet (Fig. 3a) along with blades of kyanite (Ky_2) in the leucosomes (Fig. 6c; cf. Moecher *et al.*, 2004) suggests that these two mineral varieties crystallized in the presence of a melt. This can be explained by dehydration melting of muscovite within the stability field of kyanite in pelitic and semi-pelitic lithologies according to the reaction:

$$\mathrm{Ms + Ab + Qtz \rightarrow Kfs + Ky_2 + L}, \qquad (2)$$

which must have taken place at >740 °C and pressure close to 9 kbar or more (e.g. Le Breton & Thompson, 1988). Continued heating and deformation during this stage resulted in the onset of dehydration melting of biotite according to the continuous reaction:

$$\mathrm{Bt_2 + Pl + Ky + Qtz \rightarrow Grt + Kfs + L}, \qquad (3)$$

followed by the growth of sillimanite ($Sill_1$) at the expense of kyanite (reaction 4; Fig. 12) as the *P–T* path crossed into the stability field of sillimanite, evidenced by the occurrence of sillimanite rimming kyanite in some leucosomes (Fig. 6c). Dehydration melting of biotite continued to produce more melt according to the continuous reaction:

$$\mathrm{Bt_2 + Pl + Sill_1 + Qtz \rightarrow Grt + Kfs + L}, \qquad (3b)$$

which would explain the occurrence of oriented inclusions of sillimanite ($Sill_1$) in garnet in pelitic and quartzofeldspathic schists and gneisses (Fig. 3b). In Mg-rich metagreywackes, biotite dehydration melting produced orthopyroxene (with inclusions of quartz

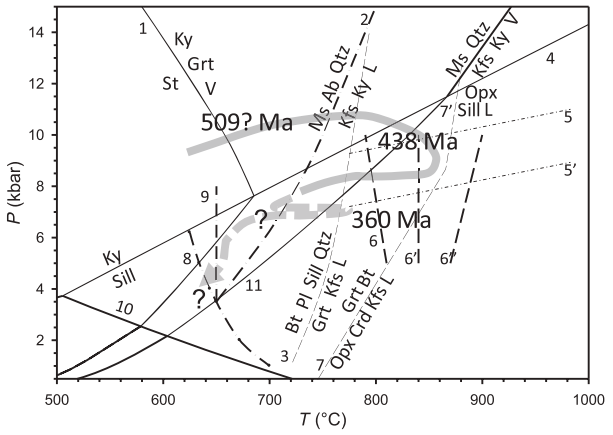

Fig. 12. *P–T*-time evolution of the Winding Stair Gap rocks based on the observed textural relations, and chemical ages for monazite. All reaction labels are as in Fig. 7.

and biotite, Fig. 6g) at >800 °C according to the experiments of Stevens *et al*. (1997) (reactions 6–6′; Fig. 12). The occurrence of some diatexites with garnet ± sillimanite, interpreted to have formed during this stage, also suggests that biotite dehydration melting was at least significant if not extensive (Brown, 2002). Accordingly, peak pressures of ~10–11 kbar at ~780–800 °C were attained, followed by a stage of heating and decompression to reach peak temperatures of 850–875 °C at 9 ± 1 kbar (Figs 7, 11 & 12). A stage of heating and (slight?) decompression is indicated by the partial replacement of rutile by ilmenite, and garnet by sillimanite$_2$ along its rim (Fig. 5e) according to the pressure-sensitive reaction (e.g. Bohlen *et al*., 1983):

$$\mathrm{Grt} + \mathrm{Rt} \rightarrow \mathrm{Ilm} + \mathrm{Sill}_2. \qquad (5)$$

This stage was accompanied by strong deformation that led to the development of the main foliation S_2 (Hatcher, 1979; Absher & McSween, 1985), and relatively rapid removal of melt.

Although it is difficult to relate precisely each of the monazite growth zones to specific stages of the *P–T–t* evolution of WSG rocks without identifying the monazite–forming reactions, we suggest that zone 2 monazite grew close to peak pressures (10–11 kbar, 780–800 °C) at *c*. 450–430 Ma. This suggestion is reasonable because monazite with significant volumes of zone 2 (e.g. Sp1Mnz1; Fig. S2a–c) is commonly included in garnet, which suggests that monazite zone 2 growth either pre-dated or coincided with garnet crystallization, most likely through biotite dehydration melting (reactions 3 & 3b). Because the growth of zone 2 monazite during these stages probably coincided with melt production and crystallization of garnet, this zone is not as Y–rich as zone 1. It is also reasonable to conclude that the melt produced during these stages was removed rapidly, preventing it from completely equilibrating with monazite, which would explain the relatively low Th/U ratio of zone 2 monazite (Rubatto *et al*., 2001). Rapid extraction of this melt led to the preservation of most garnet (cf. White & Powell, 2002), and was probably responsible for the production of features like the plagioclase-rich dykes that are either ptygmatically folded or appear to cut across the main foliation of units younger than the Ridge Pole formation exposed in other outcrops of the Central Blue Ridge.

After peak temperatures were attained, the rocks underwent a stage of near-isobaric cooling through 760–800 °C (as indicated by garnet-biotite rim re-equilibration/Fe–Mg closure temperatures; Table S1), probably in response to the rapid partial withdrawal of melt as the terrane was deforming. Cooling and slight decompression to *P–T* conditions of ~700 °C, 7 kbar followed (Fig. 12), possibly triggered by underplating (e.g. Davy & Gillet, 1986). During this stage, some of the melt remaining in place probably reacted with garnet, partially consuming it to produce biotite, sillimanite, and plagioclase (cf. reaction 3b), which appear in rinds around many garnet (Fig. 3c; Brown, 2002), while the remainder of the melt crystallized plagioclase and retrograde muscovite (Fig. 5d) in leucosomes of the stromatic metatexites. The common occurrence of late muscovite and rarity of K-feldspar in leucosomes suggest that these near isobaric cooling/slight decompression + cooling stages along a 'hair-pin' like *P–T* path (Fig. 12) occurred at pressures close to 7 kbar (but definitely at >4 kbar; cf. Spear *et al*., 1999; Brown, 2002; Pyle & Spear, 2003). Monazite was probably resorbed during this stage (Fig. 11), which would account for the irregular outlines of zone 2 areas. Processes occurring during near isobaric cooling probably took place as the area was still under the same stress regime responsible for producing the main foliation (S_2 defined by Bt_{2b} and $Sill_2$; Fig. 11).

The growth of significant volumes of monazite at *c*. 360–350 Ma on matrix crystals some of which contain inclusions of garnet, sillimanite and biotite (e.g. Fig. S5d) and mostly in the main foliation plane (S_2) suggests that the WSG area was affected by a second thermal event, as it seems unlikely for such volumes of monazite to grow during cooling. This event probably took place by near-isobaric heating to temperatures below the closure temperature of monazite, and overall lower peak *P–T* conditions (~750 °C, 7 kbar?) compared with the 450–430 Ma event, as indicated by the preservation of older ages in monazite zones 1 and 2. The growth of zone 3 monazite probably took place in the presence of a hydrothermal fluid which would explain their high Th/U. The low Y content of this zone could be explained by simultaneous crystallization of another Y-bearing phase (xenotime?), or overall low budget of available Y having been consumed by garnet (e.g. Pyle *et al*., 2005; Foster *et al*., 2002; Spear & Pyle, 2002). The hydrothermal fluid also facilitated the development of zone 3 rims on some monazite

inclusions in garnet along microfractures (e.g. Sp1Mnz1 and Sp3Mnz2; Fig. S2), and may have also led to the development of fibrolite ($Sill_3$) and myrmekite along plagioclase grain boundaries as albite was dissolved (Fig. 5f; cf. Vernon, 1979; Moecher *et al.*, 2005). This thermal pulse was probably responsible for the formation of ilmenite and hematite at the expense of magnetite in WSG-14 (Fig. 6e) according to the reaction:

$$\mathrm{Mgt} + \mathrm{Rt} \rightarrow \mathrm{Ilm} + \mathrm{Hm}$$

calculated at 743 ± 44 °C, 7 ± 1 kbar using THERMOCALC (WSG14_12*; Table S1). Because matrix monazite crystals areally dominated by zone 3 portions are elongated in the foliation plane (S_2), this 360–350 Ma thermal event likely took place while the area was under the same stress regime that prevailed earlier.

Following this thermal pulse, the WSG probably underwent a second stage of near-isobaric cooling during which garnet and orthopyroxene were partially replaced by biotite and/or chlorite, and anthophyllite/cummingtonite respectively, along rims and fractures. Yittrium released by the retrograde replacement of garnet by biotite and chlorite was incorporated in growing xenotime and monazite in the form of the thin, outermost, discontinuous rims represented by zone 5 (e.g. Parrish, 1990; Gibson *et al.*, 2004; Mahan *et al.*, 2006), whereas Ca and the REE were incorporated in allanite crystals that occur along garnet rims in some samples (e.g. WSG-2). Near-isobaric cooling was probably followed by a stage of cooling and decompression (Fig. 12) giving rise to a 'composite and stepped *P–T* path' as is commonly reported for many granulites in collisional terranes (e.g. Brown, 2002 and references therein). Finally, as the rocks cooled to temperatures below 650 °C, exsolution lamellae of ilmenite developed in Ti-hematite (Fig. 6e; cf. Absher & McSween, 1985).

TECTONIC IMPLICATIONS

The *P–T–t* path discussed above indicates that the WSG area has had a complex metamorphic history with at least two main tectonothermal events. The first of these two events was characterized by a clockwise *P–T* path reaching peak temperatures of 850 ± 30 °C at 9 ± 1 kbar 430–450 Ma. This Late Ordovician-Early Silurian event coincided with the 'Salinic Orogeny' (450–423 Ma; van Staal, 2006) of the Northern and Central Appalachians (but of which there is no record in the Southern Appalachians), and barely overlaps with the Taconic orogeny (480–450 Ma), known to be diachronous in the Central and Southern Appalachians (e.g. Hatcher, 1989; Hatcher *et al.*, 2004, 2005). This event resulted in significant partial melting, and may have overprinted some earlier arc–continent collisional event of limited areal extent that had occurred *c.* 500 Ma (as indicated by the monazite ages for zone 1). The exact reason for this metamorphic event is unknown, and our age data cannot conclusively resolve its precise timing. On one hand, if the weighted average age of 438 ± 4.5 Ma is considered correct, then the most likely cause of this metamorphic event would be the subduction of the Cartoogechaye terrane underneath Laurentia along a west-dipping subduction zone, similar to subduction events of the Salinic Orogeny recorded in the northern Appalachians (van Staal, 2006). In this case, the Cartoogechaye terrane may have been part of the northern Appalachians, consistent with the models of Dennis (2007). On the other hand, if an age of 460 ± 12 Ma (Moecher *et al.*, 2004) is considered more representative of this metamorphic event, then it may have been caused by subduction of the Cartoogechaye terrane underneath another (more distal) terrane/island arc such as the Dahlonega Gold Belt, and/or the Tugaloo terrane along an east-dipping subduction zone during the Taconic orogeny. However, according to Hatcher *et al.* (2005), the Dahlonega Gold belt is overthrust by the Cartoogechaye terrane, whereas the Tugaloo terrane is inferred to have been accreted at a much later stage during the Acadian Orogeny. In contrast, Hibbard (2000) and Hibbard *et al.* (2002) considered the docking of the Tugaloo terrane to Laurentia a Taconic event, leaving 'subduction' of the Cartoogechaye terrane along an east-dipping subduction zone as a viable possibility.

Following peak metamorphism during this Salinic/Taconic event, the melt was extracted fairly rapidly, aided by the strong compressional deformation that continued to prevail at this stage. Rapid extraction of most of the melt allowed the WSG rocks to undergo near isobaric cooling at considerable depth (~25 km) to temperatures of ~750 °C. Exhumation of the Cartoogechaye terrane was later initiated probably as a result of vertical and/or lateral extrusion (e.g. Thompson *et al.*, 1997; Wintsch *et al.*, 1999; Štípská *et al.*, 2004) by underthrusting of the Dahlonega Gold Belt along another west-dipping thrust while the entire belt was under compression.

The second metamorphic event that affected the WSG rocks was represented by a thermal pulse at 360 ± 5 Ma. Although the timing of this event coincides with the Neo-Acadian Orogeny of Hatcher (1989), this orogeny is not recorded in the Cartoogechaye terrane, Dahlonega Gold Belt, or western part of the Tugaloo terrane. The monazite age results presented in this study therefore represent the first record of Neoacadian metamorphism in the Central Blue Ridge. The fact that this thermal event was weaker than the Salinic/Taconic metamorphism and was not accompanied by major deformation suggests that it may have been related to hydrothermal activity caused by the intrusion of magma (at depths > 20 km), rather than by the major deformation recorded in the Inner Piedmont during this orogeny. This is consistent with the intrusion of granitoids such as the Yonah Mountain tonalite located 33 miles to the southwest of WSG

and intruded at 346 ± 17 Ma (Mapes, 2002), or the Spruce Pine Pegmatites intruded at 7–11 kbar (Swanson & Veal, 2010) 361 ± 2 Ma (Mapes, 2002). Following this thermal event, the Cartoogechaye terrane continued to be exhumed as the Dahlonega Gold belt continued to be underthrust beneath it, possibly facilitated by the emplacement of the Tugaloo terrane (Hatcher *et al*., 2005), and/or the docking of the Carolina Superterrane into the Laurentian margin.

If the Cartoogechaye terrane had been subducted beneath Laurentia during the Salinic orogeny, then we envision that by the time of the Alleghanian collision of Africa with Laurentia at *c*. 280 Ma, the Cartoogechaye terrane could have been exhumed to a level which allowed it to be overthrust onto the Western Blue Ridge province along an east-dipping thrust (the Hayseville fault?). However, the event seems to have had little if any metamorphic effect on the WSG rocks and the rest of the Blue Ridge terrane, probably because they were located too far inland. The common orientation of many metamorphic minerals interpreted to have crystallized at different stages of evolution of the WSG in the same foliation plane (S_2; Fig. 11) suggests that all these post-Taconic metamorphic stages (corresponding to monazite zones 3 and 5) took place under the same stress regime. Because many of these post-Taconic stages were retrogressive, we suggest that exhumation of these high grade rocks occurred primarily under compressional stress during convergence.

ACKNOWLEDGEMENTS

Detailed and insightful reviews of an earlier form of this paper by F. Spear and D. Pattison have led to a major revision of this manuscript, and are greatly appreciated. Careful reviews by K. Mahan and B. Miller, and editorial handling by M. Brown have helped us improve this work substantially. Any remaining errors are the sole responsibility of the authors. AES thanks L. Raymond for introducing him to the Geology of the southern Appalachians, and kindly providing him with S9110. Discussions with R. Hatcher during a field trip through the Blue Ridge were very informative and improved AES's understanding of the area. A. Steele and D. Neff are thanked for assistance with SEM analysis at Marshall University. This project was partly supported by funds from Marshall University to AES.

REFERENCES

Absher, B.S. & McSween, H.Y., 1985. Granulites at Winding Stair Gap, North Carolina: the thermal axis of Paleozoic metamorphism in the southern Appalachians. *Geological Society of America Bulletin*, **96,** 588–599.

Afifi, A.M. & Essene, E.J., 1988. MINFILE: a microcomputer program for storage and manipulation of chemical data on minerals. *American Mineralogist*, **73,** 446–447.

Åmli, R. & Griffin, W.L., 1975. Microprobe analysis of REE minerals using empirical correction factors. *American Mineralogist*, **60,** 599–606.

Berman, R.G., 1991. Thermobarometry using multi-equilibrium calculations: a new technique, with petrological applications. *Canadian Mineralogist*, **29,** 833–855.

Berman, R.G., 2007. winTWQ (version 2.3): a software package for performing internally-consistent thermobarometric calculations. *Geological Survey of Canada*, Open File 5462.

Bohlen, S.R. & Liotta, J.J., 1986. A barometer for garnet amphibolites and garnet granulites. *Journal of Petrology*, **27,** 1025–1034.

Bohlen, S.R., Wall, V.J. & Boettcher, A.L., 1983. Experimental investigations and geological applications of equilibria in the system: FeO–TiO_2–Al_2O_3–SiO_2–H_2O. *American Mineralogist*, **68,** 1049–1058.

Brown, M., 2002. Retrograde processes in migmatites and granulites revisited. *Journal of Metamorphic Geology*, **20,** 25–40.

Carpenter, R.H., 1970. Metamorphic history of the Blue Ridge Province of Tennessee and North Carolina. *Geological Society of America Bulletin*, **81,** 749–762.

Castaing, R., 1960. Electron probe microanalaysis. In: *Advances in Electronics and Electron Physics* (ed. Marton, L.), Vol. 13, pp. 317–386. Academic Press, New York.

Cherniak, D.J. & Watson, E.B., 2001. Pb diffusion in zircon. *Chemical Geology*, **172,** 5–24.

Cherniak, D.J., Watson, B.E., Grove, M. & Harrison, T.M., 2004. Pb diffusion in monazite: a combined RBS/SIMS study. *Geochimica et Cosmochimica Acta*, **68,** 829–840.

Cochérie, A. & Albaréde, F., 2001. An improved U-Th-Pb age calculation for electron microprobe dating of monazite. *Geochimica et Cosmochimica Acta*, **76,** 4509–4522.

Dallmeyer, R.D., 1975. Incremental $^{40}Ar/^{39}Ar$ ages of biotite and hornblende from retrograded basement gneisses of the southern Blue Ridge: their bearing on the age of Paleozoic metamorphism. *American Journal of Science*, **275,** 444–460.

Davy, P. & Gillet, P., 1986. The stacking of thrust slices in collision zones and its thermal consequences. *Tectonics*, **6,** 913–929.

Dennis, A.J., 2007. Cat Square basin, Catskill clastic wedge: Silurian-Devonian orogenic events in the central Appalachians and the crystalline southern Appalachians. In: *Whence the Mountains? Inquiries into the Evolution of Orogenic Systems: A Volume in Honor of R. A. Price: Denver* (eds Sears, J.W., Harms, T.A. & Evenchick, C.A.), *Geological Society of America*, Special Paper, **433,** 313–329.

Eckert, J.O., 2002. Monazite EMPA dates from the amphibolite-granulite metamorphic progression to the Wayah granulite core, western North Carolina: confirmation of Taconian peak metamorphism. *Geological Society of America*, Abstracts with programs, North-Central and Southeastern Sections, Joint Annual Meeting, **34,** 69 pp.

Eckert, J.O., Hatcher, R.D. & Mohr, D.W., 1989. The Wayah granulite facies metamorphic core, southwestern North Carolina: high-grade culmination of Taconic metamorphism in the southern Blue Ridge. *Geological Society of America Bulletin*, **101,** 1434–1447.

Fitzsimons, I.C.W. & Harley, S.L., 1994. The influence of retrograde cation exchange on granulite P-T estimates and a convergence technique for the recovery of peak metamorphic conditions. *Journal of Petrology*, **35,** 543–576.

Force, E.R., 1976. Metamorphic source rocks of titanium placer deposits – a geochemical cycle. *United States Geological Survey Professional Paper*, **959-B,** 16.

Foster, G., Kinny, P., Vance, D., Prince, C. & Harris, N., 2000. The significance of monazite U-Th-Pb age data in metamorphic assemblages; a combined study of monazite and garnet chronometry. *Earth and Planetary Science Letters*, **181,** 327–340.

Foster, G., Gibson, H.D., Parrish, R., Horstwood, M., Fraser, J. & Tindle, A., 2002. Textural, chemical and isotopic insights into the nature and behavior of metamorphic monazite. *Chemical Geology*, **191,** 183–207.

Gibson, H.D., Carr, S.D., Brown, R.L. & Hamilton, M.A., 2004. Correlations between chemical and age domains in monazite, and metamorphic reactions involving major pelitic phases: an integration of ID-TIMS and SHRIMP geochronology with Y-Th-U X-ray mapping. *Chemical Geology*, **211,** 237–260.

Guidotti, C., 1984. Micas in metamorphic rocks. *Reviews in Mineralogy and Geochemistry*, **13,** 357–467.

Hames, W. & Menard, T., 1993. Fluid assisted modification of garnet composition along rims, cracks, and mineral inclusion boundaries in samples of amphibolites facies schists. *American Mineralogist*, **78,** 338–344.

Harley, S.L., 1984. The solubility of alumina in orthopyroxene coexisting with garnet in FeO-MgO-Al_2O_3-SiO_2 and CaO-FeO-MgO-Al_2O_3-SiO_2. *Journal of Petrology*, **25,** 665–696.

Harrison, T.M., Catlos, E.J. & Montel, J.-M., 2002. U-Th-Pb dating of phosphate minerals. In: *Phosphates, Geochemical, Geobiological, and Materials Importance* (eds Kohn, M.J., Rakovan, J. & Hughes, J.M.), *Reviews in Mineralogy and Geochemistry*, **48,** 524–558.

Hatcher, R.D., 1973. Basement versus cover rocks in the Blue Ridge of northeast Georgia, northwestern South Carolina and adjacent North Carolina. *American Journal of Science*, **273,** 671–685.

Hatcher, R.D., 1979. The Coweeta Group and Coweeta syncline: major features of the North Carolina – Georgia Blue Ridge. *Southeastern Geology*, **21,** 17–29.

Hatcher, R.D., 1989. Tectonic synthesis of the U.S. Appalachians. *Geological Society of America*, **F2,** 511–535.

Hatcher, R.D., 2002. An inner Piedmont primer. In: *Inner Piedmont Geology in the South Mountains – Blue Ridge Foothills and the Southwestern Brushy Mountains, Central Western North Carolina* (eds Hatcher, R.D. & Bream, B.R.), Carolina Geological Society Guidebook, pp. 1–18, Raleigh, North Carolina.

Hatcher, R.D., 2010. *Southeastern Tennessee – Western North Carolina Blue Ridge: Upper to Lower Crust, 480 Million Year-old Ocean Crust and Mantle, and the 2000 m Crest of the Appalachians*. Post-Goldschmidt Conference Field trip Guide. Tectonics and Structural Geology Research Science Alliance Center of Excellence, University of Tennessee, Knoxville.

Hatcher, R.D. & Butler, J.R., 1979. *Guidebook for Southern Appalachian Field Trip in the Carolinas, Tennessee and Northeastern Georgia: International Geologic Correlation Program Project 27*. University of North Carolina, Chapel Hill, 117 pp.

Hatcher, R.D., Bream, B.R., Miller, C.F., Eckert, J.O., Fullagar Paul, D. & Carrigan, C.W., 2004. Paleozoic structure of internal basement massifs, southern Appalachian Blue Ridge, incorporating new geochronologic, Nd and Sr isotopic, and geochemical data. *Geological Society of America, Memoir*, **197,** 525–547.

Hatcher, R.D., Merschat, A.J. & Thigpen, J.R., 2005. Blue Ridge primer. *Carolina Geological Society*, Annual Field Trip, 1–24.

Hermann, J. & Rubatto, D., 2003. Relation zircon and monazite domains to garnet growth zones: age and duration of granulite facies metamorphism in the Val Malenco lower crust. *Journal of Metamorphic Geology*, **21,** 833–852.

Hibbard, J., 2000. Docking Carolina: Mid-Paleozoic accretion in the southern Appalachians. *Geology*, **28,** 127–130.

Hibbard, J.P., Stoddard, E.F., Secor, D.T. & Dennis, A.J., 2002. The Carolina Zone: overview of Neoproterozoic to Early Paleozoic peri-Gondwanan terranes along the eastern flank of the southern Appalachians. *Earth-Science Reviews*, **57,** 299–339.

Hodges, K.V. & Spear, F.S., 1982. Geothermometry, geobarometry and the Al_2SiO_5 triple point at Mt. Moosilauke, New Hampshire. *American Mineralogist*, **67,** 1118–1134.

Holdaway, M. & Lee, S.M., 1977. Fe–Mg cordierite stability in high-grade pelitic rocks based on experimental, theoretical, and natural observations. *Contributions to Mineralogy and Petrology*, **63,** 175–198.

Holland, T.J.B. & Powell, R., 2005. AX: a program to calculate activities of mineral endmembers from chemical analyses. Available at: http://www.esc.cam.ac.uk/research/research-groups/holland/ax (last accessed on 19 November 2010).

Kingsbury, J., Miller, C., Wooden, J. & Harrison, M., 1993. Monazite paragenesis and U-Pb systematic in rocks of the eastern Mojave Desert, California, USA: implications for thermochronometry. *Chemical Geology*, **110,** 147–167.

Kohn, M.J. & Malloy, M.A., 2004. Formation of monazite via prograde metamorphic reactions among common silicates: implications for age determinations. *Geochimica et Cosmochimica Acta*, **68,** 101–113.

Kretz, R., 1983. Symbols for rock forming minerals. *American Mineralogist*, **68,** 277–279.

Le Breton, N. & Thompson, A.B., 1988. Fluid-absent (dehydration) melting of biotite in metapelites in the early stages of crustal anatexis. *Contributions to Mineralogy and Petrology*, **99,** 226–237.

Loehn, C.W., 2009. *Monazite Geochronology of the Madison Mylonite Zone and Environs, Southwestern Montana with Implications for Precambrian Thermotectonic Evolution of the Northern Wyoming Province*. Unpublished MS thesis, Virginia Polytechnic Institute and State University, Blacksburg, VA.

Ludwig, K.R., 2003. *Users Manual for Isoplot/*Ex v. 3.0, A Geochronological Toolkit for Microsoft Excel. Berkley Geochronology Center Special Publication No. 4, Berkeley, CA.

Mahan, K.H., Goncalves, P., Williams, M.L. & Jercinovic, M.J., 2006. Dating metamorphic reactions and fluid flow: application to exhumation of high-*P* granulites in a crustal-scale shear zone, western Canadian Shield. *Journal of Metamorphic Geology*, **24,** 193–217.

Mapes, R.W., 2002. *Geochemistry and Geochronology of Mid-Paleozoic Granite Plutonism in the Southern Appalachian Piedmont Terrane, North Carolina–South Carolina–Georgia*. MS thesis, Vanderbilt University, Nashville, 150 pp.

Massey, M.A. & Moecher, D.P., 2005. Deformation and metamorphic history of the Western Blue Ridge – Eastern Blue Ridge terrane boundary, southern Appalachian Orogen. *Tectonics*, **24,** TC5010, doi: 10.1029/2004TC001643, 1–18.

McIntyre, G.A., Brooks, C., Compston, W. & Turek, A., 1966. The statistical assessment of Rb-Sr isochrons. *Journal of Geophysical Research*, **71,** 5459–5468.

McLellan, E., Linder, D. & Thomas, J., 1989. Multiple granulite facies events in the southern Appalachians, USA. In: *Evolution of Metamorphic Belts* (eds Daly, J.S., Cliff, R.A. & Yardley, B.W.D.), *Geological Society Special Publication*, **43,** 309–314.

Miller, C.F., Gorisch, E.B., Harrison, T.M., Coath, C.D. & Hatcher, R.D., 1996. Elucidating complex crustal histories through combined zoning and U-Th-Pb ion probe studies of zircon and monazite: an example from the Blue Ridge, NC-GA. *EOS Transactions of the American Geophysical Union*, **V31E-01,** 3635.

Miller, C.F., Hatcher, R.D., Harrison, T.M., Coath, C.D. & Gorisch, E.B., 1998. Cryptic crustal events elucidated through zone imaging and ion microprobe studies of zircon, southern Appalachian Blue Ridge, North Carolina-Georgia. *Geology*, **26,** 419–422.

Moecher, D.P., 2000. P-T Conditions and timing of peak Taconian granulite facies metamorphism in the Southern Blue Ridge, 2000. *Geological Society of America*, Annual Meeting, Reno, Nevada, **32,** 113 pp.

Moecher, D.P. & Sharp, Z.D., 1999. Comparison of conventional and garnet-aluminosilicate-quartz O isotope thermometry: insights for mineral equilibration in metamorphic rocks. *American Mineralogist*, **84,** 1287–1303.

Moecher, D.P., Samson, S.D. & Miller, C.F., 2004. Precise time and conditions of peak Taconian Granulite facies metamorphism in the southern Appalachian Orogen, USA, with implications for zircon behavior during crustal melting events. *Journal of Geology*, **112,** 289–304.

Moecher, D.P., Massey, M.A. & Tracy, R.J., 2005. Timing and pattern of metamorphism in the western and central Blue

Ridge, TN and NC: status and outstanding problems. *Carolina Geological Society*, Annual Field Trip, 57–66.
Montel, J.-M., Foret, S., Veschambre, M., Nicollet, C. & Provost, A., 1996. Electron microprobe dating of monazite. *Chemical Geology*, **131,** 37–53.
Montel, J.-M., Kornprobst, J. & Vielzeuf, D., 2000. Preservation of old U-Th-Pb ages in shielded monazite: example from the Beni Bousera Hercynian kinzigites (Morocco). *Journal of Metamorphic Geology*, **18,** 335–342.
Parrish, R., 1990. U-Pb dating of monazite and its application to geological problems. *Canadian Journal of Earth Science*, **27,** 1431–1450.
Pattison, D.R.M. & Bégin, N.J., 1994. Zoning patterns in orthopyroxene and garnet in granulites: implications for geothermometry. *Journal of Metamorphic Geology*, **12,** 387–410.
Pattison, D.R.M., Chacko, T., Farquhar, J. & McFarlane, C.R.M., 2003. Temperatures of granulite-facies metamorphism: constraints from experimental phase equilibria and thermobarometery corrected for retrograde exchange. *Journal of Petrology*, **44,** 867–900.
Perkins, E.H., Brown, T.H. & Berman, R.G., 1986. PTX-system: three programs for calculation of P-T composition phase diagrams. *Computers and Geosciences*, **12,** 749–755.
Philpotts, A.R., 1990. *Principles of Igneous and Metamorphic Petrology*. Prentice Hall, Old Tappan, NJ, 498 pp.
Pommier, A., Cochérie, A. & Legendre, O., 2003. 'EPMA DATING': a program for age calculation from electron microprobe measurements of U-Th-Pb, Geophysical Research Abstracts, 5, 09054. *European Geophysical Society*. http://adsabs.harvard.edu/abs/2003EAEJA (last accessed on xx March 2011).
Pouchou, J.L. & Pichoir, F., 1991. Quantitative analysis of homogeneous or stratified microvolumes applying the model 'PAP'. In: *Electron Probe Quantitation* (eds Heinrich, K.F.J. & Newbury, D.E.), pp. 31–75. Plenum Press, New York.
Powell, R. & Holland, T.J.B., 1994. Optimal geothermometry and geobarometry. *American Mineralogist*, **79,** 120–133.
Powell, R. & Holland, T.J.B., 2002. Course Notes for 'THERMOCALC Workshop 2002: calculating Metamorphic Phase Equilibria' (Barcelona) on CD-ROM.
Pyle, J.M. & Spear, F.S., 2003. Four generations of accessory-phase growth in low-pressure migmatites from SW New Hampshire. *American Mineralogist*, **88,** 338–8351.
Pyle, J.M., Spear, F.S., Cheney, J.T. & Layne, G., 2005. Monazite ages in the Chesham Pond Nappe, SW New Hampshire, USA: implications for assembly of central New England Thrust Sheets. *American Mineralogist*, **90,** 592–606.
Ratcliffe, N.M., Aleinikoff, J.N., Armstrong, T.R., Walsh, G.J. & Hames, W.E., 2001. Intrusive relations and isotopic ages of Devonian granites in Southern and Central Vermont: evidence for a prolonged Acadian Orogeny and partitioning of compressional strain. *Geological Society of America*, Abstracts with Programs, **33,** 32.
Reche, J. & Martinez, F.J., 1996. GPT: an Excel spreadsheet for thermobarometric calculations in metapelitic rocks. *Computers & Geosciences*, **22,** 775–784.
Richard, L.R. & Clarke, D.B., 1990. AMPHIBOL: a program for calculating structural formulae and for classifying and plotting chemical analyses of amphiboles. *American Mineralogist*, **75,** 421–423.
Rubatto, D., Williams, I. & Buick, I., 2001. Zircon and monazite response to prograde metamorphism in the Reynolds Range, central Australia. *Contributions Mineralogy and Petrology*, **140,** 458–468.
Smith, H.A. & Barreiro, B., 1990. Monazite U-Pb dating of staurolite grade metamorphism in pelitic schists. *Contributions Mineralogy and Petrology*, **105,** 602–615.
Spear, F.S., 1993. *Metamorphic Phase Equilibria and Pressure-Temperature-Time Paths*. Mineralogical Society of America, Washington D.C., 799 pp.
Spear, F.S. & Cheyney, J.T., 1989. A petrogenetic grid for pelitic schists in the system SiO_2–Al_2O_3–FeO–MgO–K_2O–H_2O. *Contributions to Mineralogy and Petrology*, **101,** 149–164.
Spear, F.S. & Florence, F.P., 1992. Thermobarometry in granulites: pitfalls and new approaches. *Precambrian Research*, **55,** 209–241.
Spear, F.S. & Kohn, M.J., 1996. Trace element zoning in garnet as a monitor of crustal melting. *Geology*, **24,** 1099–1102.
Spear, F.S. & Peacock, S.M., 1989. *Metamorphic pressure-temperature-time paths*, Short Course in Geology, 7. American Geophysical Union, Washington, DC, 102 pp.
Spear, F.S. & Pyle, J.M., 2002. Apatite, monazite, and xenotime in metamorphic rocks. In: *Phosphates, Geochemical, Geobiological, and Materials Importance* (eds Kohn, M.J., Rakovan, J. & Hughes, J.M.), *Reviews in Mineralogy and Geochemistry*, **48,** 293–335.
Spear, F.S., Kohn, M.J. & Cheney, J.T., 1999. P-T paths from anatectic pelites. *Contributions to Mineralogy and Petrology*, **134,** 17–32.
van Staal, C.R., 2006. Magmatism during the Salinic, Acadian and Neoacadian Orogenies. *Geological Society of America*, Northeast Section, Abstracts with Programs, **38**(2), 31.
Stevens, G., Clemens, J.D. & Droop, G.T.R., 1997. Melt production during granulite-facies anatexis: experimental data from 'primitive' metasedimentary protoliths. *Contributions to Mineralogy and Petrology*, **128,** 352–370.
Štípská, P., Schulmann, K. & Kröner, A., 2004. Vertical extrusion and mid-crustal spreading of omphacite granulite: a model of syn-convergent exhumation (Bohemian Massif, Czech Republic). *Journal of Metamorphic Geology*, **22,** 179–198.
Suzuki, K. & Adachi, M., 1991. The chemical U-Th-total Pb isochron ages of zircon and monazite from the Grey Granite of the Hida Terrane, Japan. *The Journal of Earth Sciences*, **38,** 11–37, Nagoya University.
Swanson, S.E. & Veal, W.B., 2010. Mineralogy and petrogenesis of pegmatites in the Spruce Pine District, North Carolina, USA. *Journal of Geosciences*, **55,** 27–42.
Thompson, A.B., 2001. Clockwise P-T paths for crustal melting and H_2O recycling in granite source regions and migmatite terrains. *Lithos*, **56,** 33–45.
Thompson, J.B. & Thompson, A.B., 1976. A model system for mineral facies in pelitic schists. *Contributions Mineralogy and Petrology*, **58,** 243–277.
Thompson, A.B., Schulmann, K. & Jezek, J., 1997. Extrusion tectonics and elevation of lower crustal metamorphic rocks in convergent orogens. *Geology*, **25,** 491–494.
Tomkins, H.S. & Pattison, D.R.M., 2007. Accessory phase petrogenesis in relation to major phase assemblages in pelites from the Nelson contact aureole, southern British Columbia. *Journal of Metamorphic Geology*, **25,** 401–421.
Tracy, R.J., 1982. Compositional zoning and inclusions in metamorphic minerals. *Reviews in Mineralogy and Geochemistry*, **10,** 355–397.
Tracy, R.J. & Loehn, C.W., 2006. SHRIMP versus electron microprobe monazite ages: direct comparison of isotopic vs. chemical dating, and the implications for geologic interpretation. *Geological Society of America*, Abstracts with Programs, **38,** 63.
Tracy, R.J., Loehn, C.W., Dahl, P.S. *et al*., 2005. Direct comparison of monazite ages obtained by in-situ techniques: ion-probe isotopic ages versus electron microprobe chemical ages. *EOS Transactions of the American Geophysical Union*, **86**(52), Fall Meeting Supplement, Abstract V13A-0517.
Turner, F.J., 1981. *Metamorphic Petrology*, 2nd edn. McGraw Hill Publishing Company, New York, 524 pp.
Vernon, R.H., 1979. Formation of late sillimanite by hydrogen metasomatism (base leaching) in some high grade gneisses. *Lithos*, **12,** 143–152.
Wendt, I. & Carl, C., 1991. The statistical distribution of the mean squared weighted deviation. *Chemical Geology*, **86,** 275–285.

White, R.W. & Powell, R., 2002. Melt loss and the preservation of granulite facies mineral assemblages. *Journal of Metamorphic Geology*, **20,** 621–632.

White, R.W., Powell, R. & Holland, T.J.B., 2001. Calculation of partial melting equilibria in the system Na_2O-CaO-K_2O-FeO-MgO-Al_2O_3-SiO_2-H_2O (NCKFMASH). *Journal of Metamorphic Geology*, **19,** 139–153.

Williams, M.L., Jercinovic, M.J. & Terry, M.P., 1999. Age mapping and dating of monazite on the electron microprobe: deconvoluting multistage tectonic histories. *Geology*, **27,** 1023–1026.

Wing, B.A., Ferry, J.M. & Harrison, T.M., 2003. Prograde destruction and formation of monazite and allanite during contact and regional metamorphism of pelites: petrology and geochronology. *Contributions to Mineralogy and Petrology*, **145,** 228–250.

Wintsch, R.P., Byrne, T. & Toriumi, M., 1999. Exhumation of the Sanbagawa blueschist belt, SW Japan, by lateral flow and extrusion: evidence from structural kinematics and retrograde P-T-t paths. In: *Exhumation Processes: Normal Faulting, Ductile Flow and Erosion* (eds Ring, U., Brandon, M.T., Lister, G.S. & Willett, S.D.), *Geologcal Society of London, Special Publications*, **154,** 129–155.

Zhu, X.K. & O'Nions, R.K., 1999. Zonation of monazite in metamorphic rocks and its implications for high temperature thermochronology: a case study from the Lewisian terrain. *Earth and Planetary Science Letters*, **171,** 209–220.

SUPPORTING INFORMATION

Additional Supporting Information may be found in the online version of this article:

Figure S1. Biotite compositions in quartzofeldspathic gneisses and granofelses (a & b); pelitic schists (c & d); and orthopyroxenites and garnet–biotite–hornblende granofelses (e & f).

Figure S2. Chemical zones and age domains of dated monazite inclusions in garnet, sample WSG-14. (a) U, Th, Y and distribution of chemical zones 1 through 5 for Sp1 Mnz1; (b) chemical ages for Sp1 Mnz1; (c) probability density plot showing average ages with 2σ errors and MSWD obtained from 'weighted average age plots' for Sp1 Mnz1 using 'ISOPLOT/Ex v. 3.0' (Ludwig, 2003); (d) U, Th and Y X-ray maps, and distribution of chemical zones 1 through 5 for Sp3 Mnz2; (e) Chemical ages for Sp3 Mnz2; (f) probability density plot showing average ages with 2σ errors and MSWD obtained from 'weighted average age plots' for Sp3 Mnz2 using 'ISOPLOT/Ex v. 3.0' (Ludwig, 2003). All chemical zone patterns are as in (a).

Figure S3. Chemical zones and age domains of Mnz 6, sample WSG-14. (a) U, Th and Y X-ray maps, and distribution of chemical zones 1 through 5 (b) chemical ages for Mnz 6 showing some age domains that correspond to the chemical zones, and the locations of the age and chemical profiles A–A′ through D–D′; (c)–(f) age and chemical zoning profiles along the lines A–A′ through D–D′. Typical uncertainties on individual spot analyses range from ±25 to ±100 Ma; (g) probability density plot showing average ages with 2σ errors and MSWD obtained from 'weighted average age plots' for Mnz6 using 'ISOPLOT/Ex v. 3.0' (Ludwig, 2003);

Figure S4. Chemical zones and age domains of Mnz 10, sample WSG-14. (a) U, Th and Y X-ray maps, and distribution of chemical zones 1 through 5 (b) and (c) Age and chemical zoning profiles along the lines A–A′ through B–B′ respectively; (d) probability density plot showing average ages with 2σ errors and MSWD obtained from 'weighted average age plots' for Mnz 10 using 'ISOPLOT/Ex v. 3.0' (Ludwig, 2003).

Figure S5. Chemical zones and age domains of two monazite crystals embedded in matrix plagioclase, sample WSG-14. (a) U, Th and Y X-ray maps, and distribution of chemical zones 1 through 5 for monazite crystal Sp2 Mnz 1; (b) Age and chemical zoning profiles along the line A–A′; (c) probability density plot showing average ages with 2σ errors obtained from 'weighted average age plots' for Sp2 Mnz1 using 'ISOPLOT/Ex v. 3.0' (Ludwig, 2003); (d) U, Th and Y X-ray maps, and distribution of chemical zones 1 through 5 for monazite crystal Mnz 8 containing inclusions of garnet, biotite and sillimanite, and mantled by plagioclase (e) and (f) Age and chemical zoning profiles along the lines C–C′ and E–E′ respectively; (g) probability density plot showing average ages with $2\sigma\sigma$ errors obtained from 'weighted average age plots' for Sp1 Mnz1 using 'ISOPLOT/Ex v. 3.0' (Ludwig, 2003).

Figure S6. Chemical zones and age domains of Mnz 7, sample WSG-14. (a) U, Th and Y X-ray maps, and distribution of chemical zones 1 through 5 (b) chemical zones for Mnz 7 and corresponding average age for the dominant zone 3; (c) and (d) age and chemical zoning profiles along the lines A–A′ and B–B′ respectively; (e) probability density plot for Mnz 7; (f) weighted mean age and MSWD obtained from the statistical treatment of all ages for Mnz 7 using 'ISOPLOT/Ex v. 3.0' (Ludwig, 2003); (g) CHIME Th*–Pb diagram (Suzuki & Adachi, 1991) yielding an age of 349 ± 33 Ma for Mnz 7.

Table S1. Optimal Thermobarometric Results for the Widing Stair Gap Samples based on the approach of Powell & Holland (1994) calculated using THERMOCALC 3.26.

Appendix S1. Monazite data used for age analysis.

Appendix S2. BSEI showing samples of analytical points used for thermobarometric calculations.

Appendix S3. Monazite data eliminated from final age analysis.

Please note: Wiley-Blackwell are not responsible for the content or functionality of any supporting materials supplied by the authors. Any queries (other than missing material) should be directed to the corresponding author for the article.

Received 18 August 2010; revision accepted 7 March 2011.